PHYSICAL REVIEW B **106**, 155142 (2022)

Flat-band ferromagnetism in a correlated topological insulator on a honeycomb lattice

Leonardo S. G. Leite and R. L. Doretto

Instituto de Física Gleb Wataghin, Universidade Estadual de Campinas, 13083-859 Campinas, SP, Brazil

(Received 1 April 2022; revised 30 September 2022; accepted 5 October 2022; published 21 October 2022)

We study the flat-band ferromagnetic phase of a spinfull and time-reversal symmetric Haldane-Hubbard model on a honeycomb lattice within a bosonization formalism for flat-band Z_2 topological insulators. Such a study extends our previous one [Phys. Rev. B **104**, 155129 (2021)] concerning the flat-band ferromagnetic phase of a correlated Chern insulator described by a Haldane-Hubbard model. We consider the topological Hubbard model at $1/4$ filling of its corresponding noninteracting limit and in the nearly flat band limit of its lower free-electronic bands. We define boson operators associated with two distinct spin-flip excitations, one that changes (mixed-lattice excitations) and a second one that preserves (same-lattice excitations) the index related to the two triangular sublattices. Within the bosonization scheme, the fermion model is mapped into an effective interacting boson model, whose quadratic term is considered at the harmonic approximation in order to determine the spin-wave spectrum. For both mixed- and same-lattice excitations, we find that the spin-wave spectrum is gapped and has two branches, with an energy gap between the lower and the upper bands at the K and K' points of the first Brillouin zone. We find that the same-lattice excitations are indeed the lowest-energy (elementary) excitations that characterize the flat-band ferromagnetic phase, a feature that contrasts with the behavior of a previously studied correlated topological insulator on a square lattice, whose flat-band ferromagnetic phase is characterized by mixed-lattice excitations. We also find some evidences that the spin-wave bands for the same-lattice excitations might be topologically nontrivial even in the completely flat band limit.

DOI: 10.1103/PhysRevB.106.155142

I. INTRODUCTION

The first theoretical proposal of a Chern band insulator came from a pioneering work of Haldane in 1988 [1]. In that paper, Haldane introduced a spinless tight-binding model on a honeycomb lattice with broken time-reversal symmetry that even without an external source of magnetic field displays a quantum Hall effect. The emergence of this distinct insulating quantum Hall phase derives from the topologically nontrivial electronic band structure of the Haldane model: the nonzero Chern numbers [2] of these electronic bands yield a finite Hall conductivity at half-filling, i.e., the system exhibits the so-called anomalous quantum Hall effect [3,4].

The Haldane model on a honeycomb lattice was later geneneralized by Kane and Mele [5,6], providing the first microscopic model for a topological insulator [7,8]. Here the spin degree of freedom is explicitly included and, in contrast with Haldane model, time-reversal symmetry is preserved. Although at half filling time-reversal symmetry yields a vanishing total Chern number, such a system may exhibit a quantum spin Hall effect [5,6,9]. Indeed, the Kane-Mele model is an example of a Z_2 topological insulator, a system which is characterized by a Z_2 invariant that distinguishes between the trivial insulator phase and the topologically nontrivial one [7,8]. In spite of the fact that the Kane-Mele model is not experimentally realized so far, the quantum spin Hall effect was theoretically predicted [10] and later experimentally observed [11] in HgTe/CdTe quantum wells at low temperatures. Interestingly, experimental implementations of topological insulators using ultracold atoms in optical lattices have also been considered [12–14].

Correlation effects on topological insulators have also been receiving some attention in recent years [15,16]. An interesting example of a correlated topological insulator on a honeycomb lattice is the Kane-Mele-Hubbard model [17–26], which is a generalization of the Kane-Mele model with the electron-electron interaction being described by an on-site Hubbard repulsion term. The phase diagram of the model has been determined [17,20,21] at half filling. In particular, quantum Monte Carlo simulations have been performed [20,21], since, in this case, the so-called fermion sign problem is absent, a feature that is related to the fact that the model preserves particle-hole symmetry at half filling [20]. It was shown that, apart from some possible intermediate phases, a Z_2 topological band insulator phase survives for small to moderate values of the on-site repulsion energy U and that the system enters a magnetically ordered phase above a critical on-site repulsion energy U_c. An analytical description of such Mott transition was recently performed [26].

Another set of interacting topological systems that has been recently gaining some attention is made out of lattice models that display (nearly) flat and topologically nontrivial electronic bands in the noninteracting limit [27–34]. In a sense, these papers transport the long discussed subject of flat-band ferromagnetism [35–37] to the realm of lattice models with topologically nontrivial free-electronic bands. Indeed, the merging of these two subjects was motivated by a series of papers [38–40] that describe tight-binding models, specially in two dimensions, with only short-range hoppings and whose parameters, once fine tuned, may yield nearly flat and topologically nontrivial electronic bands. In particular, in Ref. [34], we studied the flat-band ferromagnetic (FM) phase of a correlated Chern insulator on a honeycomb lattice described by a Haldane-Hubbard model. We considered the model at $1/4$ filling (half filling of the lower and doubly degenerated free-electronic band) and in the vicinity of a suitable choice of the model parameters [38], that yields nearly flat noninteracting bands. In order to describe such a flat-band FM phase, we employed a bosonization scheme for flat-band correlated Chern insulators [29], that was developed by one of us. Such a formalism allows us to map the Haldane-Hubbard model to an effective interacting boson model: We considered the effective boson model within a harmonic approximation and determined the spin-wave spectrum; it was found that the excitation spectrum has one gapped and one gapless excitation branches, with a Goldstone mode at the center of the first Brillouin zone (a feature that indicates the stability of the flat-band FM phase) and Dirac points at the K and K' points of the first Brillouin zone (BZ).

In the present paper, we extend our previous study [34] about the flat-band FM phase of a correlated Chern insulator on a honeycomb lattice, by considering a similar, but now time-reversal symmetric, topological Hubbard model (THM) model on a honeycomb lattice. The noninteracting term of such correlated Z_2 topological insulator is given by a spinfull version of the Haldane model [1] that preserves time-reversal symmetry. Similarly to Ref. [34], we consider the THM at $1/4$ filling of its noninteracting limit and in the vicinity of the nearly flat band limit [38] of its lower free-electronic band. The flat-band FM phase of the time-reversal symmetric THM is described within a bosonization scheme for flat-band correlated Z_2 topological insulators, a formalism that was introduced in Ref. [29] and is based on the bosonization formalism [41] proposed to study the quantum Hall system at filling factor $\nu = 1$. Again, the THM is mapped to an effective interacting boson model. We define boson operators [Eq. (26)] associated with two distinct spin-flip excitations that are termed mixed-lattice [Eq. (28)] and same-lattice [Eq. (33)] excitations. In both cases, we find that the spin-wave excitation spectrum is gapped and constituted by two bands completely separated from each other, a feature that contrasts with the spin-wave spectrum of the correlated Chern insulator [34], whose bands touch at the corners of the first BZ. Interestingly, in contrast with the square lattice correlated topological insulator [29], whose flat-band FM phase is characterized by mixed-lattice excitations, here, for the correlated topological insulator on a honeycomb lattice, we find that the same-lattice ones are indeed the correct mode, which furnishes the lowest-energy excitations [see Figs. 2(a)–2(f)]. Finally, we also find some indications that the spin-wave excitation bands for the same-lattice excitations might be topologically nontrivial, since the corresponding Chern numbers are nonzero. As far as we know, this is the first calculation of the spin-wave spectrum for the flat-band FM phase of a correlated Z_2 topological insulator on a honeycomb lattice described by a Haldane-Hubbard like model.

Our paper is organized as follows. In Sec. II, we introduce the time-reversal symmetric THM on a honeycomb lattice. In Sec. III, the bosonization formalism for flat-band Z_2 topological insulators [29] is briefly reviewed. In Sec. IV, the effective interacting boson model, that allows us to described the flat-band FM phase of the correlated topological insulator, is presented; the boson model is considered within the harmonic approximation: the spin-wave spectrum is determined for homogeneous and sublattice dependent on-site Hubbard repulsion energies. Section V contains a brief summary of our main results. Some details of the bosonization formalism and additional results are presented in the five Appendices.

II. THE TIME-REVERSAL SYMMETRIC HALDANE-HUBBARD MODEL

In this section, we introduce a time-reversal symmetric Haldane-Hubbard model on a honeycomb lattice. Our discussion closely follows the lines of Sec. II from Ref. [34], where such a Haldane-Hubbard model with broken time-reversal symmetry is described.

A. The fermionic interacting model

Let us consider N_e spin-$1/2$ electrons on a honeycomb lattice described by a Haldane-Hubbard model, whose Hamiltonian assumes the form

$$H = H_0 + H_U, \tag{1}$$

where the noninteracting term is given by

$$\begin{aligned} H_0 = t_1 &\sum_{i \in A, \delta, \sigma} \left(c^\dagger_{iA\sigma} c_{i+\delta B\sigma} + \text{H.c.} \right) \\ + t_2 &\sum_{i \in A, \tau, \sigma} \left(e^{-i\gamma_\sigma \phi} c^\dagger_{iA\sigma} c_{i+\tau A\sigma} + \text{H.c.} \right) \\ + t_2 &\sum_{i \in B, \tau, \sigma} \left(e^{+i\gamma_\sigma \phi} c^\dagger_{iB\sigma} c_{i+\tau B\sigma} + \text{H.c.} \right), \end{aligned} \tag{2}$$

while the interacting one is an on-site Hubbard repulsion term,

$$H_U = \sum_i \sum_{a=A,B} U_a \hat{\rho}_{ia\uparrow} \hat{\rho}_{ia\downarrow}. \tag{3}$$

Here the operator $c^\dagger_{ia\sigma}$ ($c_{ia\sigma}$) creates (destroys) an electron with spin $\sigma = \uparrow, \downarrow$ on the ith site of the (triangular) sublattice $a = A, B$ of the honeycomb lattice. The nearest-neighbor and next-nearest-neighbor hopping amplitudes are both positive and given by t_1 and t_2, respectively [see Fig. 1(a)]. Indeed, the next-nearest-neighbor hopping is complex, $t_2 e^{\pm i\gamma_\sigma \phi}$, which indicates that the electron acquires a (spin-dependent) $+\gamma_\sigma \phi$ phase and a $-\gamma_\sigma \phi$ phase as it moves, respectively, in the same and opposite directions of the arrows associated with the dashed lines in Fig. 1(a) (see also note [42]). The complex next-nearest-neibhbor hopping yields a fictitious flux pattern with zero net flux per unit cell [38]. Importantly, time-reversal invariance requires that $\gamma_\uparrow = -\gamma_\downarrow = 1$, which implies that the spin $\uparrow$ electrons and the spin $\downarrow$ electrons experience an opposite fictitious flux pattern (see also Sec. II from Ref. [29]). The index δ indicates the nearest-neighbor vectors

$$\boldsymbol{\delta}_1 = -a\hat{y}, \qquad \boldsymbol{\delta}_{2,3} = \pm\frac{a}{2}\left(\sqrt{3}\hat{x} \pm \hat{y}\right), \tag{4}$$

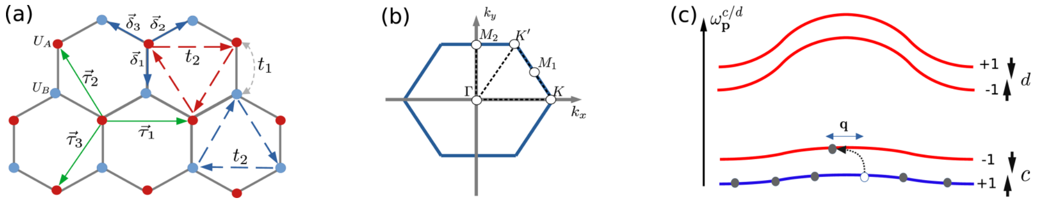

FIG. 1. (a) Schematic representation of the THM model (1) on an honeycomb lattice. Red and blue circles respectively represent the sites of the (triangular) sublattices A and B. The nearest-neighbor and next-nearest-neighbor hopping energies are given by t_1 and $t_2 e^{\pm i\phi}$ (positive sign follows arrow direction), respectively, while U_A and U_B indicate the sublattice dependent on-site Hubbard repulsion energies. The nearest-neighbor (4) and next-nearest-neighbor (5) vectors are indicate by $\boldsymbol{\delta}_i$ and $\boldsymbol{\tau}_i$, respectively. (b) The first BZ, where $\mathbf{K} = (4\pi/3\sqrt{3}, 0)$, $\mathbf{K}' = (2\pi/3\sqrt{3}, 2\pi/3)$, $\mathbf{M}_1 = (\pi/\sqrt{3}, \pi/3)$, and $\mathbf{M}_2 = (0, 2\pi/3)$, with the nearest-neighbor distance of the honeycomb lattice $a = 1$. (c) Schematic representation of the noninteracting electronic bands (16) in the nearly-flat band limit (17) of the lower bands c. At 1/4 filling, the ground state is the FM state (25) and low energy excitations are particle-hole pairs (spin flips) within the lower bands. Although the noninteracting bands c and d are doubly degenerated with respect to the spin degree of freedom, we introduce an offset between the $\sigma = \uparrow$ and $\downarrow$ bands for clarity. The Chern numbers (18) of each band are also shown on the right side.

as illustrated in Fig. 1(a), and τ corresponds to the next-nearest-neighbor vectors $\boldsymbol{\tau}_1 = \boldsymbol{\delta}_2 - \boldsymbol{\delta}_3$, $\boldsymbol{\tau}_2 = \boldsymbol{\delta}_3 - \boldsymbol{\delta}_1$, and $\boldsymbol{\tau}_3 = \boldsymbol{\delta}_1 - \boldsymbol{\delta}_2$:

$$\boldsymbol{\tau}_1 = a\sqrt{3}\hat{x}, \qquad \boldsymbol{\tau}_{2,3} = -\frac{a}{2}\left(\sqrt{3}\hat{x} \mp 3\hat{y}\right). \tag{5}$$

Hereafter, we set the nearest-neigbhor distance $a = 1$. One should mention that, for $\phi = \pi/2$, the tight-binding model (2) corresponds to the Kane-Mele model in the absence of the Rashba term [5]. Finally, $\hat{\rho}_{ia\sigma}$ is the density operator for spin σ electrons at site i of sublattice a,

$$\hat{\rho}_{ia\sigma} = c^{\dagger}_{ia\sigma} c_{ia\sigma}, \tag{6}$$

and $U_a > 0$ are the on-site and sublattice-dependent repulsion energies.

B. Diagonalization of the noninteracting Hamiltonian

In order to diagonalize the noninteracting model (2), one considers the Fourier transform

$$c^{\dagger}_{ia\sigma} = \frac{1}{\sqrt{N_a}} \sum_{\mathbf{k}\in\mathrm{BZ}} e^{i\mathbf{k}\cdot\mathbf{R}_i} c^{\dagger}_{\mathbf{k}\,a\,\sigma}, \tag{7}$$

where $N_a = N$ is the number of sites of the sublattice a and the momentum sum runs over the first BZ associated with the underline triangular Bravais lattice, see Fig. 1(b). The noninteracting Hamiltonian (2) can then be written in a matrix form, i.e.,

$$H_0 = \sum_{\mathbf{k}} \Psi^{\dagger}_{\mathbf{k}} H_{\mathbf{k}} \Psi_{\mathbf{k}}, \tag{8}$$

where the 4×4 $H_{\mathbf{k}}$ matrix reads

$$H_{\mathbf{k}} = \begin{pmatrix} h^{\uparrow}_{\mathbf{k}} & 0 \\ 0 & h^{\downarrow}_{\mathbf{k}} \end{pmatrix} \tag{9}$$

and the four-component spinor $\Psi_{\mathbf{k}}$ is defined as

$$\Psi_{\mathbf{k}} = \begin{pmatrix} c_{\mathbf{k}A\uparrow} & c_{\mathbf{k}B\uparrow} & c_{\mathbf{k}A\downarrow} & c_{\mathbf{k}B\downarrow} \end{pmatrix}^T. \tag{10}$$

The 2×2 matrices $h^{\uparrow}_{\mathbf{k}}$ and $h^{\downarrow}_{\mathbf{k}}$ associated with each spin sector in Eq. (9) can be written in terms of the identity matrix τ_0 and the vector $\hat{\tau} = (\tau_1, \tau_2, \tau_3)$, whose components are Pauli matrices, i.e.,

$$h^{\sigma}_{\mathbf{k}} = B^{\sigma}_{0,\mathbf{k}} \tau_0 + \mathbf{B}^{\sigma}_{\mathbf{k}} \cdot \hat{\tau}, \tag{11}$$

where $\mathbf{B}^{\sigma}_{\mathbf{k}} = (B^{\sigma}_{1,\mathbf{k}}, B^{\sigma}_{2,\mathbf{k}}, B^{\sigma}_{3,\mathbf{k}})$ and

$$\begin{aligned} B^{\sigma}_{0,\mathbf{k}} &= B_{0,\mathbf{k}} = 2t_2 \cos(\phi) \sum_{\tau} \cos(\mathbf{k}\cdot\boldsymbol{\tau}), \\ B^{\sigma}_{1,\mathbf{k}} &= B_{1,\mathbf{k}} = t_1 \sum_{\delta} \cos(\mathbf{k}\cdot\boldsymbol{\delta}), \\ B^{\sigma}_{2,\mathbf{k}} &= B_{2,\mathbf{k}} = t_1 \sum_{\delta} \sin(\mathbf{k}\cdot\boldsymbol{\delta}), \\ B^{\sigma}_{3,\mathbf{k}} &= \gamma_{\sigma} B_{3,\mathbf{k}} = \gamma_{\sigma}(-2t_2)\sin(\phi) \sum_{\tau} \sin(\mathbf{k}\cdot\boldsymbol{\tau}), \end{aligned} \tag{12}$$

with $\gamma_{\uparrow} = -\gamma_{\downarrow} = 1$ and the indices δ and τ corresponding to the nearest-neighbor (4) and next-nearest-neighbor (5) vectors, respectively. Although the two matrices associated with each spin sector are different, they are not independent, since time-reversal symmetry yields $h^{\uparrow}_{\mathbf{k}} = h^{\downarrow\,*}_{-\mathbf{k}}$ (see Appendix A from Ref. [29] for further details).

It is possible to diagonalize the Hamiltonian (8) with the aid of the canonical transformation

$$\begin{aligned} c_{\mathbf{k}A\uparrow} &= u^{*}_{\mathbf{k}} d_{\mathbf{k}\uparrow} + v_{\mathbf{k}} c_{\mathbf{k}\uparrow}, \quad c_{\mathbf{k}A\downarrow} = u_{-\mathbf{k}} d_{\mathbf{k}\downarrow} + v^{*}_{-\mathbf{k}} c_{\mathbf{k}\downarrow}, \\ c_{\mathbf{k}B\uparrow} &= v^{*}_{\mathbf{k}} d_{\mathbf{k}\uparrow} - u_{\mathbf{k}} c_{\mathbf{k}\uparrow}, \quad c_{\mathbf{k}B\downarrow} = v_{-\mathbf{k}} d_{\mathbf{k}\downarrow} - u^{*}_{-\mathbf{k}} c_{\mathbf{k}\downarrow}, \end{aligned} \tag{13}$$

where the coefficients $u_{\mathbf{k}}$ and $v_{\mathbf{k}}$ are given by

$$\begin{aligned} |u_{\mathbf{k}}|^2, |v_{\mathbf{k}}|^2 &= \frac{1}{2}\left(1 \pm \hat{B}_{3,\mathbf{k}}\right), \\ u_{\mathbf{k}} v^{*}_{\mathbf{k}} &= \frac{1}{2}\left(\hat{B}_{1,\mathbf{k}} + i\hat{B}_{2,\mathbf{k}}\right), \end{aligned} \tag{14}$$

with $\hat{B}_{i,\mathbf{k}}$ being the ith component of the unit vector $\hat{\mathbf{B}}_{\mathbf{k}} = \mathbf{B}_{\mathbf{k}}/|\mathbf{B}_{\mathbf{k}}|$. The diagonalized Hamiltonian reads

$$H_0 = \sum_{\mathbf{k}\sigma} \omega^{c}_{\mathbf{k}} c^{\dagger}_{\mathbf{k}\sigma} c_{\mathbf{k}\sigma} + \omega^{d}_{\mathbf{k}} d^{\dagger}_{\mathbf{k}\sigma} d_{\mathbf{k}\sigma}, \tag{15}$$

where the dispersions of the lower band c ($-$ sign) and the upper band d ($+$ sign) are given by

$$\omega^{d/c}_{\mathbf{k}} = B_0 \pm \sqrt{B^2_{1,\mathbf{k}} + B^2_{2,\mathbf{k}} + B^2_{3,\mathbf{k}}}. \tag{16}$$

Notice that both c and d free-electronic bands are doubly degenerated with respect to the spin degree of freedom. For more details, we refer the reader to Fig. 2 from Ref. [34], where the free-electronic bands (16) are plotted for different values of the parameters t_2/t_1 and ϕ.

As discussed in detail in Refs. [34,38], the noninteracting band structure (16) have quite interesting properties when the model parameters t_2/t_1 and ϕ are fine tuned. For instance, for (nearly flat band limit)

$$\phi = 0.656 \quad \text{and} \quad t_2 = 0.3155 t_1, \tag{17}$$

the lower band c and the upper band d are separated by an energy gap and the lower band c is almost flat. Away from the nearly flat band limit (17), the lower band c gets more dispersive, and, in particular, for $\phi = 0$ or $t_2 = 0$, the energy gap closes at the K and K' points of the first BZ (see Fig. 2(a) from Ref. [34]).

In vicinity of the nearly flat band limit (17), the free-electronic bands (16) are also topologically nontrivial. Indeed, for tight-binding models of the form (8), one shows that the Chern numbers of the upper and lower bands assume the form [8,13,43]

$$C^{c/d}_{\sigma} = \pm\gamma_\sigma \frac{1}{4\pi}\int_{BZ} d^2k\, \hat{\mathbf{B}}_{\mathbf{k}} \cdot (\partial_{k_x}\hat{\mathbf{B}}_{\mathbf{k}} \times \partial_{k_y}\hat{\mathbf{B}}_{\mathbf{k}}). \tag{18}$$

In particular, for the noninteracting model (2), one finds $C^d_\uparrow = -C^d_\downarrow = -1$ and $C^c_\uparrow = -C^c_\downarrow = +1$. As discussed in Sec. IV from Ref. [29], at half-filling, the so-called charge Chern number $C_{\text{charge}} = (C^c_\uparrow + C^c_\downarrow)/2 = 0$ while the spin Chern number $C_{\text{spin}} = (C^c_\uparrow - C^c_\downarrow)/2 = 1$. Since the tight-binding model (2) conserves the z-component of the total spin (see Sec. II A from Ref. [29]), the Z_2 topological invariants [8,13] for the free-electronic bands $\nu_{c/d} = C^{c/d}_{\text{spin}} \bmod 2 = \pm 1$, i.e., the tight-binding model (2) is indeed a Z_2 topological insulator. At half filling, such a system should display the quantum spin Hall effect [5,6,9] with the spin Hall conductivity $\sigma^{SH}_{xy} = eC^c_{\text{spin}}/2\pi$.

C. Interaction term in momentum space

To find the expression of the on-site Hubbard repulsion term (3) in momentum space, we start writing the Fourier transform of the electron density operator (6),

$$\hat{\rho}_{ia\sigma} = \frac{1}{N}\sum_{\mathbf{q}\in \text{BZ}} e^{i\mathbf{q}\cdot\mathbf{R}_i}\hat{\rho}_{a\sigma}(\mathbf{q}). \tag{19}$$

After substituting Eq. (19) into Eq. (3), we obtain

$$H_U = \frac{1}{N}\sum_{a=A,B}\sum_{\mathbf{q}} U_a \hat{\rho}_{a\uparrow}(-\mathbf{q})\hat{\rho}_{a\downarrow}(\mathbf{q}). \tag{20}$$

In terms of the fermion operators $c^\dagger_{\mathbf{k}\,a\,\sigma}$ [see Eq. (7)], the electron density operator $\hat{\rho}_{a\sigma}(\mathbf{q})$ reads

$$\hat{\rho}_{a\sigma}(\mathbf{q}) = \sum_{\mathbf{p}} c^\dagger_{\mathbf{p}-\mathbf{q}\,a\,\sigma} c_{\mathbf{p}\,a\,\sigma}. \tag{21}$$

Substituting Eq. (13) into (21) and neglecting the terms that contain the fermions $d_{\mathbf{k}\,\sigma}$, one finds the expression of the electron density operator (21) *projected* into the lower noninteracting bands c (see Eq. (28) from Ref. [29])

$$\bar{\rho}_{a\,\sigma}(\mathbf{q}) = \sum_{\mathbf{p}} G_{a\,\sigma}(\mathbf{p},\mathbf{q}) c^\dagger_{\mathbf{p}-\mathbf{q}\,\sigma} c_{\mathbf{p}\,\sigma}, \tag{22}$$

where the $G_{a\,\sigma}(\mathbf{p},\mathbf{q})$ functions are given by

$$\begin{aligned} G_{a\,\sigma}(\mathbf{p},\mathbf{q}) = {} & \delta_{a,A}(\delta_{\sigma,\uparrow} v^*_{\mathbf{p}-\mathbf{q}} v_{\mathbf{p}} + \delta_{\sigma,\downarrow} v_{-\mathbf{p}+\mathbf{q}} v^*_{-\mathbf{p}}) \\ & + \delta_{a,B}(\delta_{\sigma,\uparrow} u^*_{\mathbf{p}-\mathbf{q}} u_{\mathbf{p}} + \delta_{\sigma,\downarrow} u_{-\mathbf{p}+\mathbf{q}} u^*_{-\mathbf{p}}), \end{aligned} \tag{23}$$

with $u_{\mathbf{k}}$ and $v_{\mathbf{k}}$ being the coefficients (14).

Finally, we quote the expression of the on-site Hubbard term (20) projected into the lower noninteracting bands c, which follows from Eq. (20) with $\hat{\rho}_{a\sigma}(\mathbf{q}) \to \bar{\rho}_{a\sigma}(\mathbf{q})$:

$$\bar{H}_U = \frac{1}{N}\sum_{a=A,B}\sum_{\mathbf{q}} U_a \bar{\rho}_{a\uparrow}(-\mathbf{q})\bar{\rho}_{a\downarrow}(\mathbf{q}). \tag{24}$$

III. BOSONIZATION FORMALISM FOR FLAT-BAND Z_2 TOPOLOGICAL INSULATORS

Here we summarize the bosonization formalism for a Z_2 topological insulator introduced by one of us in Ref. [29] for the description of the flat-band FM phase of a square lattice correlated Z_2 topological insulator. Our discussion follows the lines of Sec. III from Ref. [34].

In order to introduce the bosonization scheme, one needs to define a reference state. Let us consider a spinfull topological insulator on a bipartite lattice whose Hamiltonian assumes the form (8), choose the model parameters such that (at least) the lower band c is (nearly) flat, and focus on the 1/4 filling of the electronic bands: the number of electrons $N_e = N_A = N_B = N$, with N_A and N_B being, respectively, the number of sites of the sublattices A and B. Assuming that the lower band $c\uparrow$ is completely occupied [see Fig. 1(c)], the ground state of the noninteracting system (the *reference* state) is completely spin polarized:

$$|\text{FM}\rangle = \prod_{\mathbf{k}\in \text{BZ}} c^\dagger_{\mathbf{k}\uparrow}|0\rangle. \tag{25}$$

Excited states are generated by spin flips: As illustrated in Fig. 1(c), the lowest-energy neutral excitations above the reference state (25) are particle-hole pairs within the lower bands c, since the lower flat bands c are separated from the upper ones d by an energy gap; such an excited state with well-defined momentum can be written as $|\Psi_{\mathbf{k}}\rangle \propto S^-_{\mathbf{k}}|\text{FM}\rangle$. Interestingly, it is possible to define boson operators that are associated with such spin-flip excitations (see Ref. [29] for details),

$$\begin{aligned} b_{\alpha,\mathbf{q}} &= \frac{\bar{S}^+_{-\mathbf{q},\alpha}}{F_{\alpha\alpha,\mathbf{q}}} = \frac{1}{F_{\alpha\alpha,\mathbf{q}}}\sum_{\mathbf{p}} g^*_\alpha(-\mathbf{p},\mathbf{q}) c^\dagger_{\mathbf{p}+\mathbf{q}\uparrow} c_{\mathbf{p}\downarrow}, \\ b^\dagger_{\alpha,\mathbf{q}} &= \frac{\bar{S}^-_{\mathbf{q},\alpha}}{F_{\alpha\alpha,\mathbf{q}}} = \frac{1}{F_{\alpha\alpha,\mathbf{q}}}\sum_{\mathbf{p}} g_\alpha(\mathbf{p},\mathbf{q}) c^\dagger_{\mathbf{p}-\mathbf{q}\downarrow} c_{\mathbf{p}\uparrow}, \end{aligned} \tag{26}$$

with $\alpha = 0, 1$, that obey the commutation relations

$$\begin{aligned} [b_{\alpha,\mathbf{k}}, b^\dagger_{\beta,\mathbf{q}}] &= \delta_{\alpha,\beta}\,\delta_{\mathbf{k},\mathbf{q}}, \\ [b_{\alpha,\mathbf{k}}, b_{\beta,\mathbf{q}}] &= [b^\dagger_{\alpha,\mathbf{k}}, b^\dagger_{\beta,\mathbf{q}}] = 0. \end{aligned} \tag{27}$$

Concerning the definition of the projected spin operators $\bar{S}^{\pm}_{\mathbf{q},\alpha}$ in Eq. (26), we consider *two distinct* proposals.

(i) *Mixed-lattice excitations*. Motivated by previous results [29] concerning a correlated Z_2 topological insulator on a square lattice, we define $\bar{S}^{\pm}_{\mathbf{q},\alpha}$ as

$$\bar{S}^{\pm}_{\mathbf{q},\alpha} = \bar{S}^{\pm}_{\mathbf{q},AB} + (-1)^{\alpha}\bar{S}^{\pm}_{\mathbf{q},BA}, \tag{28}$$

where

$$\bar{S}^{\pm}_{\mathbf{q},ab} = \bar{S}^{x}_{\mathbf{q},ab} \pm i\bar{S}^{y}_{\mathbf{q},ab}. \tag{29}$$

The operator $\bar{S}^{\lambda}_{\mathbf{q},ab}$, with $\lambda = x, y, z$ and $a, b = A, B$, is the spin operator $S^{\lambda}_{\mathbf{q},ab}$ *projected* into the lower noninteracting bands c. The spin operator $S^{\lambda}_{\mathbf{q},ab}$ is indeed the Fourier transform of the operator

$$S^{\lambda}_{i,ab} = \frac{1}{2}\sum_{\mu,\nu=\uparrow,\downarrow} c^{\dagger}_{ia\mu}\sigma^{\lambda}_{\mu\,\nu}c_{ib\nu}, \tag{30}$$

where $\sigma^{\lambda}_{\mu\,\nu}$ is the matrix element of the Pauli matrix σ^{λ}. The spin operators (28) are indeed related with spin-flip excitations that also change the sublattice index. Due to such a feature, we denote the excitations defined by the boson operators (26) and the spin operator (28) as *mixed-lattice* (ML) excitations. The $F^{2}_{\alpha\beta,\mathbf{q}}$ function reads

$$F^{2}_{\alpha\beta,\mathbf{q}} = \sum_{\mathbf{p}} g_{\alpha}(\mathbf{p},\mathbf{q})g^{*}_{\beta}(-\mathbf{p}+\mathbf{q},\mathbf{q}), \tag{31}$$

with $g_{\alpha}(\mathbf{p},\mathbf{q})$ defined in terms of the coefficients (14),

$$g_{\alpha}(\mathbf{p},\mathbf{q}) = -u_{\mathbf{p}}v_{-\mathbf{p}+\mathbf{q}} - (-1)^{\alpha}v_{\mathbf{p}}u_{-\mathbf{p}+\mathbf{q}}. \tag{32}$$

Interestingly, the $F^{2}_{\alpha\beta,\mathbf{q}}$ function can be explicitly expressed in terms of the $B_{i,\mathbf{k}}$ functions (12), see Eq. (A1).

(ii) *Same-lattice excitations*. Motivated by our previous study [34] about a honeycomb lattice correlated Chern insulator, we also consider spin-flip excitations that preserve the sublattice index. In this case, one defines

$$\bar{S}^{\pm}_{\mathbf{q},\alpha} = \bar{S}^{\pm}_{\mathbf{q},A} + (-1)^{\alpha}\bar{S}^{\pm}_{\mathbf{q},B}, \tag{33}$$

where $\bar{S}^{\pm}_{\mathbf{q},a}$ is also given by Eqs. (29) and (30) with $a = b$, i.e., $\bar{S}^{\pm}_{\mathbf{q},a} = \bar{S}^{\pm}_{\mathbf{q},aa}$; again, boson operators are defined as done in Eq. (26), with $F^{2}_{\alpha\beta,\mathbf{q}}$ also given by Eq. (31), but now $g_{\alpha}(\mathbf{p},\mathbf{q})$ assumes the form

$$g_{\alpha}(\mathbf{p},\mathbf{q}) = v_{-\mathbf{p}+\mathbf{q}}v_{\mathbf{p}} + (-1)^{\alpha}u_{-\mathbf{p}+\mathbf{q}}u_{\mathbf{p}}, \tag{34}$$

with $u_{\mathbf{k}}$ and $v_{\mathbf{k}}$ being the coefficients (14). Since the spin operators (33) preserve the sublattice index, we denote such excitations as *same-lattice* (SL) excitations. The expression of the $F^{2}_{\alpha\beta,\mathbf{q}}$ function in terms of the $B_{i,\mathbf{k}}$ functions (12) is shown in Appendix B, see Eq. (B1). Finally, one should note that, for both ML and SL excitations,

$$b_{\alpha,\mathbf{q}}|\mathrm{FM}\rangle = 0, \tag{35}$$

which indicates that the spin-polarized (reference) state (25) is indeed the vacuum for the boson operators (26), regardless the definition of the projected spin operators.

As discussed in detail in Ref. [29], it is possible to find the bosonic representation of any operator that is written in terms of the fermions $c^{\dagger}_{\mathbf{k}\sigma}$ and $c_{\mathbf{k}\sigma}$. For instance, in terms of the boson operators (26) (either defined in terms of the ML or the SL excitations), the bosonic representation of the projected electron density operator (22) reads

$$\bar{\rho}_{a\sigma}(\mathbf{k}) = \frac{1}{2}N\delta_{\sigma,\uparrow}\delta_{\mathbf{k},0} + \sum_{\alpha,\beta,\mathbf{q}}\mathcal{G}_{\alpha\beta a\sigma}(\mathbf{k},\mathbf{q})b^{\dagger}_{\beta,\mathbf{k}+\mathbf{q}}b_{\alpha,\mathbf{q}}, \tag{36}$$

where the $\mathcal{G}_{\alpha\beta a\sigma}(\mathbf{k},\mathbf{q})$ function is defined by Eq. (A2). Similar to the $F^{2}_{\alpha\beta,q}$ function (31), $\mathcal{G}_{\alpha\beta a\sigma}(\mathbf{k},\mathbf{q})$ can also be written in terms of the coefficients (12), see Eqs. (A3) and (B2) for ML and SL excitations, respectively. As discussed in the next section, both the Hamiltonian (2) and the interaction term (3), projected into the lower noninteracting bands c, can also be expressed in terms of the boson operators (26). Apart from the expressions of $F^{2}_{\alpha\beta,q}$ and $\mathcal{G}_{\alpha\beta a\sigma}(\mathbf{k},\mathbf{q})$, the bosonic representation (36) of the density operator (22) and the effective boson model [see Eq. (46) below] derived from the THM (1) are equal, regardless the nature of the excitations considered (ML or SL ones); due to such a feature, we employ the same notation for the boson operators (26) for both ML (28) and SL (33) excitations.

Finally, it is important to emphasize that, for the square lattice π-flux model [29], only the ML excitations (28) yield two sets of independent bosons operators b_0 and b_1. Such a feature distinguishes the time-reversal symmetric square lattice π-flux model from the generalized Haldane one [Eq. (2)], which, in principle, allows us to define boson operators from both ML (28) and SL (33) excitations. Interestingly, for the generalized square lattice π-flux model [29] and the generalized Haldane model [34], both with broken time-reversal symmetry, the SL excitations (33) are the lowest-energy excitations of the corresponding correlated Chern insulators.

IV. FLAT-BAND FERROMAGNETISM IN THE TOPOLOGICAL HUBBARD MODEL

In this section, we study the flat-band FM phase of the THM (1). We consider the model at 1/4 filling of its corresponding noninteracting limit and assume that the noninteracting lower bands c are in the vicinity of the nearly flat band limit (17). We focus on the determination of the dispersion relation of the elementary particle-hole pair excitations (spin-waves) above the (flat-band) FM ground state (25): ML [Eq. (28)] and SL [Eq. (33)] excitations are discussed separately, since they are two distinct proposals for the definition of the boson operators (26); most importantly, we find that the SL excitations (33) are indeed the lowest-energy excitations.

A. Effective interacting boson model

Here we derive an effective interacting boson model from the THM (1) within the bosonization formalism summarized in Sec. III. Our presentation closely follows the lines of Sec. IV A from Ref. [34] and more details can be found in Ref. [29].

First of all, we project the Hamiltonian (1) into the lower noninteracting bands c (such a restriction is justified, once the on-site repulsion energies U_a fullfil some conditions, see comment above Eq. (35) from Ref. [34]),

$$H \to \bar{H} = \bar{H}_0 + \bar{H}_U, \tag{37}$$

where the projected noninteracting Hamiltonian $\bar{H}_0$ is obtained from Eq. (15),

$$\bar{H}_0 = \sum_{\mathbf{k}\sigma} \omega^c_{\mathbf{k}} c^\dagger_{\mathbf{k}\sigma} c_{\mathbf{k}\sigma}, \tag{38}$$

and $\bar{H}_U$ is given by Eq. (24). In terms of the boson operators (26), the noninteracting (kinetic) term $\bar{H}_0$ reads

$$\bar{H}_{0,B} = E_0 + \sum_{\alpha\beta} \sum_{\mathbf{q}\in\mathrm{BZ}} \bar{\omega}^{\alpha\beta}_{\mathbf{q}} b^\dagger_{\beta,\mathbf{q}} b_{\alpha,\mathbf{q}}, \tag{39}$$

where $E_0 = \sum_{\mathbf{k}} \omega^c_{\mathbf{k}}$ is a constant related to the action of the Hamiltonian $\bar{H}_0$ into the reference state (25) and

$$\bar{\omega}^{\alpha\beta}_{\mathbf{q}} = \sum_{\mathbf{p}} \left(\omega^c_{\mathbf{p}-\mathbf{q}} - \omega^c_{\mathbf{p}}\right) \frac{g_\alpha(\mathbf{p},\mathbf{q}) g^*_\beta(-\mathbf{p}+\mathbf{q},\mathbf{q})}{F_{\alpha\alpha,\mathbf{q}} F_{\beta\beta,\mathbf{q}}}, \tag{40}$$

with $F_{\alpha\beta,\mathbf{q}}$ given by Eqs. (A1) (ML excitations) and (B1) (SL excitations) and $g_\alpha(\mathbf{p},\mathbf{q})$ given by Eqs. (32) (ML excitations) and (34) (SL excitations). The on-site Hubbard term $\bar{H}_U$ can be cast into its bosonic representation with the aid of Eqs. (24) and (36); after normal-ordering the resulting expression, one arrives at [29]

$$\bar{H}_{U,B} = \bar{H}^{(2)}_{U,B} + \bar{H}^{(4)}_{U,B}, \tag{41}$$

where the quadratic and quartic terms are given by

$$\bar{H}^{(2)}_{U,B} = \sum_{\alpha\beta} \sum_{\mathbf{q}} \epsilon^{\alpha\beta}_{\mathbf{q}} b^\dagger_{\beta,\mathbf{q}} b_{\alpha,\mathbf{q}}, \tag{42}$$

$$\bar{H}^{(4)}_{U,B} = \frac{1}{N} \sum_{\mathbf{k},\mathbf{q},\mathbf{p}} \sum_{\alpha\beta\alpha'\beta'} V^{\alpha\beta\alpha'\beta'}_{\mathbf{k},\mathbf{q},\mathbf{p}} b^\dagger_{\beta',\mathbf{p}+\mathbf{k}} b^\dagger_{\beta,\mathbf{q}-\mathbf{k}} b_{\alpha\mathbf{q}} b_{\alpha'\mathbf{p}}, \tag{43}$$

with the coefficient $\epsilon^{\alpha\beta}_{\mathbf{q}}$ assuming the form

$$\begin{aligned} \epsilon^{\alpha\beta}_{\mathbf{q}} = {} & \frac{1}{2} \sum_a U_a \mathcal{G}_{\alpha\beta a\downarrow}(0,\mathbf{q}) \\ & + \frac{1}{N} \sum_{a,\alpha',\mathbf{k}} U_a \mathcal{G}_{\alpha'\beta a\uparrow}(-\mathbf{k},\mathbf{k}+\mathbf{q}) \mathcal{G}_{\alpha\alpha' a\downarrow}(\mathbf{k},\mathbf{q}), \end{aligned} \tag{44}$$

and the boson-boson interaction being defined by

$$V^{\alpha\beta\alpha'\beta'}_{\mathbf{k},\mathbf{q},\mathbf{p}} = \frac{1}{N} \sum_a U_a \mathcal{G}_{\alpha\beta a\uparrow}(-\mathbf{k},\mathbf{q}) \mathcal{G}_{\alpha'\beta' a\downarrow}(\mathbf{k},\mathbf{p}). \tag{45}$$

One should recall that, in terms of the coefficients (12), the $\mathcal{G}_{\alpha\beta a\sigma}(\mathbf{k},\mathbf{q})$ functions are given by Eqs. (A3) and (B2) for ML and SL excitations, respectively. In summary, the effective *interacting* boson model, which allows us to describe the flat-band FM phase of the THM (1), reads

$$\bar{H}_B = \bar{H}_{0,B} + \bar{H}^{(2)}_{U,B} + \bar{H}^{(4)}_{U,B}. \tag{46}$$

It is important to emphasize that the effective boson model (46) is quite general, since, in principle, it can describe the flat-band FM phase of a correlated Z_2 topological insulator described by a THM on a bipartite lattice, as long as its corresponding noninteracting term assumes the form (8) and its free-electronic bands can be made almost dispersionless by carefully choosing the model parameters (see Sec. V from Ref. [34] for more details): recall that, all terms of the Hamiltonian (46) can be written in terms of the functions (12), which completely characterize tight-binding models of the form (8).

B. Spin-wave spectrum

We now determine the spin-wave spectrum of the flat-band FM phase of the THM (1) with the aid of the effective boson model (46). In the lowest-order (harmonic) approximation, the Hamiltonian (46) reads

$$\bar{H}_B \approx \bar{H}_{0,B} + \bar{H}^{(2)}_{U,B}. \tag{47}$$

The Hamiltonian (47) can be diagonalized with the aid of the following canonical transformation

$$b_{0,\mathbf{q}} = u^*_{\mathbf{q}} a_{+,\mathbf{q}} + v_{\mathbf{q}} a_{-,\mathbf{q}}, \quad b_{1,\mathbf{q}} = v^*_{\mathbf{q}} a_{+,\mathbf{q}} - u_{\mathbf{q}} a_{-,\mathbf{q}}. \tag{48}$$

One then easily shows that

$$\bar{H}_B = E_0 + \sum_{\mu=\pm} \sum_{\mathbf{q}\in BZ} \Omega_{\mu,\mathbf{q}} a^\dagger_{\mu,\mathbf{q}} a_{\mu,\mathbf{q}}, \tag{49}$$

where the constant $E_0 = \sum_{\mathbf{k}} \omega^c_{\mathbf{k}} = (-1.69\, t_1)N$ for the nearly flat band limit (17), the dispersion relation $\Omega_{\mu,\mathbf{q}}$ of the bosons $a_\pm$ (the spin-wave spectrum) is given by

$$\Omega_{\pm,\mathbf{q}} = \frac{1}{2}\left(\epsilon^{00}_{\mathbf{q}} + \epsilon^{11}_{\mathbf{q}}\right) \pm \epsilon_{\mathbf{q}}, \tag{50}$$

with $\epsilon_{\mathbf{q}} = \frac{1}{2}\sqrt{(\epsilon^{00}_{\mathbf{q}} - \epsilon^{11}_{\mathbf{q}})^2 + 4\epsilon^{01}_{\mathbf{q}}\epsilon^{10}_{\mathbf{q}}}$, and the coefficients $u_{\mathbf{q}}$ and $v_{\mathbf{q}}$ satisfy the relations

$$\begin{gathered} |u_{\mathbf{q}}|^2, |v_{\mathbf{q}}|^2 = \frac{1}{2} \pm \frac{1}{4\epsilon_{\mathbf{q}}}\left(\epsilon^{00}_{\mathbf{q}} - \epsilon^{11}_{\mathbf{q}}\right), \\ u_{\mathbf{q}} v^*_{\mathbf{q}} = \frac{\epsilon^{01}_{\mathbf{q}}}{4\epsilon_{\mathbf{q}}}, \quad v_{\mathbf{q}} u^*_{\mathbf{q}} = \frac{\epsilon^{10}_{\mathbf{q}}}{4\epsilon_{\mathbf{q}}}. \end{gathered} \tag{51}$$

Note that the vacuum state for the bosons $a_\pm$ is the ground state of the Hamiltonian (49). Indeed, due to the form of the canonical transformation (48), one sees that the vacuum for the bosons $a_\pm$ corresponds to the spin-polarized ferromagnet state (25), which is the vacuum (reference) state for the bosons b_0 and b_1 [see Eq. (35)]. Such a result points to the stability of a flat-band FM phase for the THM (1).

The spin-wave spectra (50) for the ML excitations (28) are shown in Figs. 2(a)–2(c), while the results for the SL ones (33) are displayed in Figs. 2(d)–2(f) and 3(a) and 3(b). In the following, we concentrate on the spin-wave spectrum for the SL excitations, since they are the lowest-energy excitations that characterize the flat-band FM phase of the THM (1). A detailed discussion about the ML excitations can be found in Appendix C.

SL excitations

In order to determine the spin-wave spectrum (50) for the SL excitations (33), one needs to calculate the kinetic coefficients (40) and the coefficients (44) associated with the quadratic term (42). In this case, one should consider the expressions of the $g_\alpha(\mathbf{p},\mathbf{q})$, $F_{\alpha\beta,\mathbf{q}}$, and $\mathcal{G}_{\alpha\beta a\sigma}(\mathbf{p},\mathbf{q})$ functions given by Eqs. (34), (B1), and (B2), respectively. Differently from the ML excitations (see Appendix C), for the SL excitations, one finds that the kinetic coefficients (40) vanishes, $\bar{\omega}^{\alpha\beta}_{\mathbf{q}} = 0$. Moreover, the quadratic term (42) of the effective boson model (46) is Hermitian, since the coefficients $\epsilon^{\alpha\alpha}_{\mathbf{q}}$ are real quantities while $\epsilon^{01}_{\mathbf{q}}$ and $\epsilon^{10}_{\mathbf{q}}$ are complex ones with $\epsilon^{01}_{\mathbf{q}} = (\epsilon^{10}_{\mathbf{q}})^*$ [see Eq. (44) and Fig. 6(c)]; such a feature

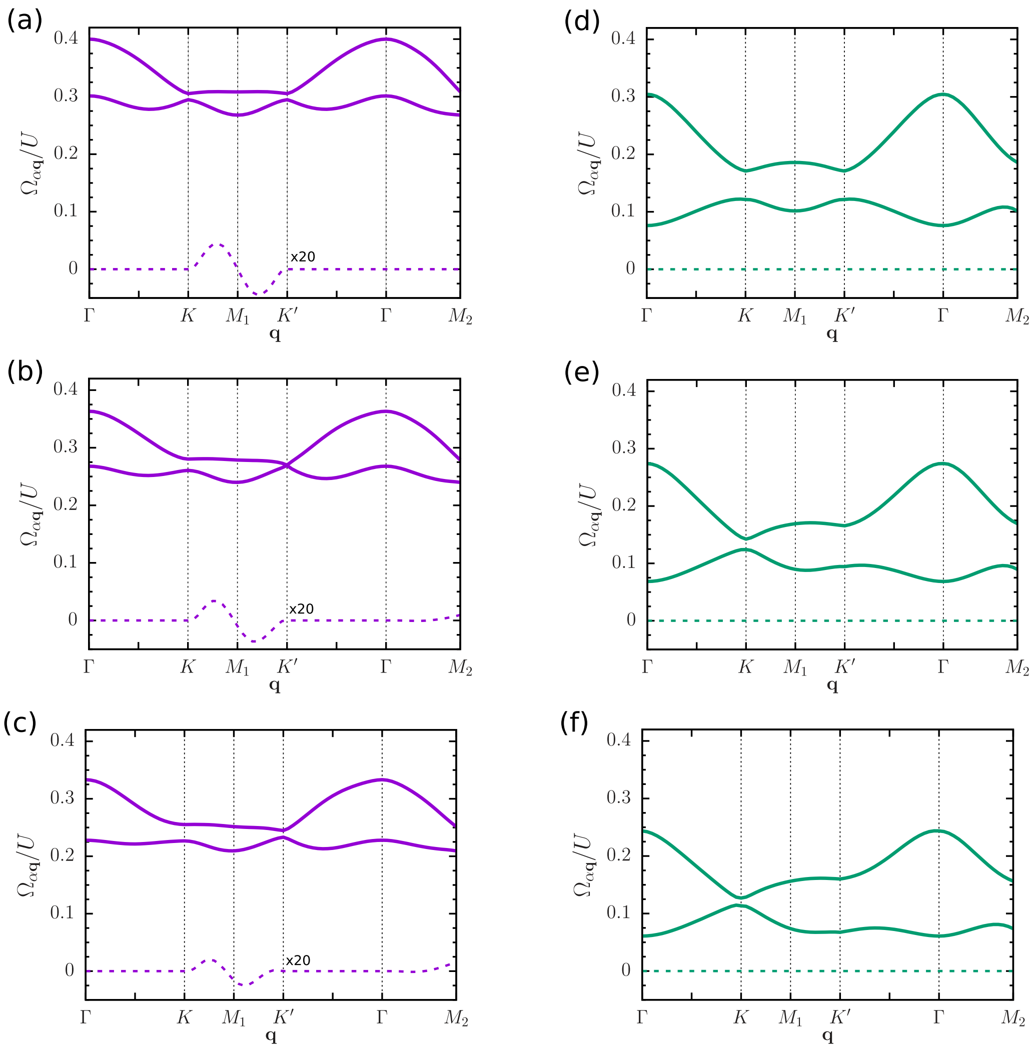

FIG. 2. Dispersion relation (50) (spin-wave spectrum) of the effective boson model (47) in the harmonic approximation for the nearly flat band limit (17) along paths in the first BZ [Fig. 1(b)]. Solid and dashed lines respectively represent the real part of $\Omega_{\pm,\mathbf{q}}$ and the imaginary part of $\Omega_{+,\mathbf{q}} = -\Omega_{-,\mathbf{q}}$, where the latter is multiplied by a factor of 20 for clarity. The spin-wave spectrum (solid magenta line) for the ML excitations (28) are shown in (a)–(c), while (d)–(f) correspond to the spin-wave spectrum (solid green line) for the SL excitations (33). The on-site Hubbard repulsion energies are $U_A = U_B = U$ [(a) and (d)], $U_B = 0.8\,U_A = 0.8\,U$ [(b) and (e)], and $U_B = 0.6\,U_A = 0.6\,U$ [(c) and (f)].

is distinct from the ones found for the ML excitations (see Appendix C) and for the correlated Chern insulator [34], whose corresponding quadratic Hamiltonians (42) are non-Hermitian. Finally, similarly to the ML excitations (see Fig. 4) and the correlated Chern insulator [34], one finds that the condition

$$F_{\alpha\beta,\mathbf{q}} = \delta_{\alpha,\beta} F_{\alpha\alpha,\mathbf{q}} \tag{52}$$

is not fulfilled for all momenta within the first BZ [see Figs. 6(a) and 6(b)]; the validity of the condition (52) is an important ingredient for the definition (26) of the two sets of *independent* boson operators b_0 and b_1; for a detailed discussion about this important issue, we refer the reader to Appendix C and to Appendix B from Ref. [34].

The dispersion relation (50) [the spin-wave spectrum for the SL excitations (33)] for the nearly flat band limit (17) and on-site repulsion energies $U_A = U_B = U$ is shown in Fig. 2(d). Notice that, instead of the nearest-neighbor hopping energy t_1, the energy scale of the spin-wave spectrum is given by the on-site repulsion energy U, since the kinetic coefficients (40) (associated with the noninteracting bands c) are neglected. Similarly to the ML excitations [Fig. 2(a)], the spin-wave spectrum for the SL excitations is also gapped and has two branches: the gap of the lower branch is at the Γ point of the first BZ while the gap of upper one is at the K and K' points. In contrast with the correlated Chern insulator [34], whose spin-wave spectrum has a Goldstone mode at the Γ point related to a continuous SU(2) symmetry that is spontaneously broken, the flat-band FM phase of the correlated topological insulator (1) has a gapped spectrum: such a feature, that is properly described by the bosonization formalism, is due to the fact that both the Hamiltonian (1) and the ground state (25) preserve a U(1) spin rotation symmetry (see Sec. II A from Ref. [29] and Ref. [28] for more details). Differently from the corresponding correlated Chern insulator [34], whose spin-wave spectrum has Dirac points at the K and K' points, here one finds an energy gap between the lower and upper bands at the K and K' points,

$$\Delta^{(K)} = \Omega_{+,K} - \Omega_{-,K} = 4.96 \times 10^{-2}\, U; \tag{53}$$

such a gap is large than the one [Eq. (C1)] found for the ML excitations. Interestingly, apart from the energy gaps at the Γ, K, and K' points, the spin-wave spectrum shown in Fig. 2(d) qualitatively resembles the one of the correlated Chern insulator on the honeycomb lattice that we have previously studied (see Fig. 6(a) from Ref. [34]). Finally, since the quadratic boson term (42) is Hermitian, the spin-wave excitations (50) are real quantities, i.e., the decay rates of the spin-wave excitations vanish, in contrast with the behavior of the ML excitations, which display a quite small decay rate [see Figs. 2(a) and 2(d)]. Importantly, for each momentum within the first BZ, the excitation energy associated with the upper band of the SL case is lower than the corresponding value of the ML case, a feature also found for the lower bands [see Figs. 2(a) and 2(d)]. Therefore the SL excitations are indeed the lowest-energy excitations that characterize the flat-band FM phase of the THM (1), a feature that contrasts with the square lattice correlated Z_2 topological insulator [29], whose elementary excitations of the corresponding flat-band FM phase are of the ML type.

In addition to the THM (1) with homogeneous on-site repulsion energies $U_A = U_B = U$, the spin-wave spectrum with a sublattice dependent on-site energy U_a was also determined. We show the spin-wave spectrum (50) for the nearly flat-band limit (17) and $U_B = 0.8\,U_A = 0.8\,U$ and $U_B = 0.6\,U_A = 0.6\,U$ in Figs. 2(e) and 2(f), respectively. Similarly to the ML excitations [Figs. 2(b) and 2(c)], we find that a finite $\Delta U = U_A - U_B$ modifies the spin-wave spectrum as compare to the homogeneous case $U_A = U_B = U$. In particular, it breaks the symmetry at the K and K' points displayed by the spin-wave spectrum in the homogeneous case. Such an asymmetry at the K and K' points of the spin-wave spectrum as ΔU increases was also found for the correlated Chern insulator [34] and it might be related to the fact that a Hubbard term with $U_A \neq U_B$ breaks inversion symmetry. Notice that, as the diference ΔU increases: The energies of the spin-wave excitations decrease; the energy gap between the lower and upper bands at the K point decreases,

$$\Delta^{(K)} = 1.82 \times 10^{-2}\, U \quad \text{for} \quad \Delta U = 0.2\, U,$$
$$\Delta^{(K)} = 1.34 \times 10^{-2}\, U \quad \text{for} \quad \Delta U = 0.4\, U,$$

while the one at the K' point increases,

$$\Delta^{(K')} = 7.11 \times 10^{-2}\, U \quad \text{for} \quad \Delta U = 0.2\, U,$$
$$\Delta^{(K')} = 9.26 \times 10^{-2}\, U \quad \text{for} \quad \Delta U = 0.4\, U.$$

For $U_B > U_A$ (not shown here), similar features are observed, but now the energy gap at the K point increases instead of the one at the K' point. Again, similarly to the homogeneous case, the energies of spin-wave spectrum of the SL case are lower than the corresponding ones of the ML case for a fixed ΔU.

We also investigate how the spin-wave spectrum (50) modifies as the THM (1) is tuned away from the nearly flat band limit (17), once the next-nearest-neighbor hopping amplitude t_2 and the phase ϕ are modified while the on-site Hubbard energies U_a are kept fixed. As mentioned in Sec. II B(see also Fig. 2 from Ref. [34]), the noninteracting electronic bands c [Eq. (16)] become more dispersive as the model (1) moves away from the nearly flat band limit (17). In the following, we describe the effects on the spin-wave spectrum only due to variations of the parameters t_2 and ϕ. We refer the reader to Appendix D for a similar discussion concerning the effects of a finite staggered on-site energy term in the Hamiltonian (1).

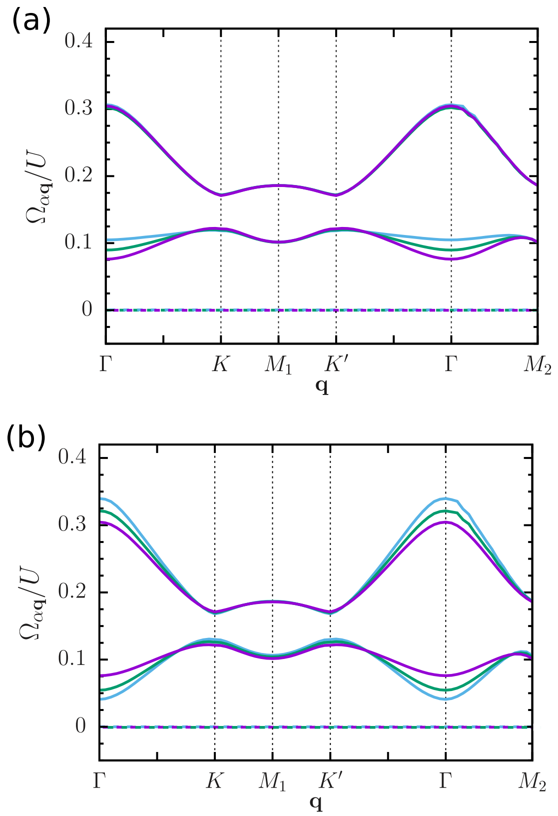

FIG. 3. SL excitations (33). Spin-wave spectrum (50) along paths in the first BZ for on-site repulsion energies $U_A = U_B = U$ and the next-nearest-neighbor hopping amplitude t_2 given by $\cos(\phi) = t_1/(4t_2)$. Solid and dashed lines respectively represent the real part of $\Omega_{\pm,\mathbf{q}}$ and the imaginary part of $\Omega_{+,\mathbf{q}} = -\Omega_{-,\mathbf{q}}$. Phase $\phi = 0.4$ [blue line in (a)], $\phi = 0.5$ [green line in (a)], $\phi = 0.656$ (magneta line), $\phi = 0.7$ [green line in (b)], and $\phi = 0.8$ [blue line in (b)].

In Fig. 3(a), it is shown the spin-wave spectrum (50) for $\phi = 0.656$, 0.7, and 0.8, hopping amplitude t_2 determined by $\cos(\phi) = t_1/(4t_2)$, and on-site repulsion energies $U_A = U_B = U$. We find that the spin-wave spectrum (in units of the on-site Hubbard energy U) for $\phi = 0.7$ and 0.8 is rather similar to the one for the nearly-flat band limit (17), which corresponds to $\phi = 0.656$. As the parameter ϕ increases, one sees that only the excitation energies of the lower band in the vicinity of the Γ point increases while the rest of the spectrum remains almost the same as compared with the one obtained for the nearly flat band limit (17). Indeed, for $\phi = 0.8$, the energy gap of the lower band moves from the Γ to the M_i points. On the other hand, as shown in Fig. 3(b), a decreasing of the parameter ϕ from $\phi = 0.656$ yields: A decreasing of the excitation energies of the lower band in the vicinity of the Γ point; an increasing of the excitation energies of the upper

TABLE I. Chern numbers of the lower spin-wave bands (50) for both the ML (C_{ML}) and the SL (C_{SL}) excitations at the nearly flat band limit (17).

	$U_A = U_B = U$	$U_B = 0.8\,U_A = 0.8\,U$
C_{ML}	± 0.29	± 0.18
C_{SL}	± 1.17	± 1.08

band around the same point; and a small decreasing in the energy gap between the lower and upper bands at the K and K' points. Indeed, one finds that such energy gap $\Delta^{(K)} = \Omega_{+,K} - \Omega_{-,K} = 3.81 \times 10^{-2}\,U$ ($\phi = 0.4$), $4.35 \times 10^{-2}\,U$ ($\phi = 0.5$), $4.96 \times 10^{-2}\,U$ ($\phi = 0.656$), $5.19 \times 10^{-2}\,U$ ($\phi = 0.7$), and $5.34 \times 10^{-2}\,U$ ($\phi = 0.8$). We believe that such rather small modifications in the spin-wave spectrum as the model (1) is tuned away from the nearly flat band limit (17) might be due to the fact that the main effects associated with the dispersion of the lower noninteracting band c, that are encoded in the kinetic coefficients (40), are not properly taken into account by the bosonization scheme.

Concerning the topological properties of the spin-wave bands, we find some evidences that the spin-wave bands for the SL excitations (33) might be topologically nontrivial. In Table I, we present the Chern numbers C_{SL} of the lower spin-wave bands (50) for the SL excitations shown in Figs. 2(d) and 2(e) [the corresponding Chern numbers C_{ML} for the ML excitations shown in Figs. 2(a) and 2(b) are also included for comparison]. Such a feature contrasts with the one found for the corresponding correlated Chern insulator on a honeycomb lattice [32,34], whose spin-wave bands are topologically trivial in the completely flat band limit. For more details about the topological properties of the spin-wave bands, we refer the reader to Appendix E.

V. SUMMARY

In summary, in this paper we studied the flat-band FM phase of a correlated Z_2 topological insulator on a honeycomb lattice described by a topological Hubbard model, whose noninteracting limit is given by a generalization of the spinless Haldane model [1]. Such a study complements our previous one [34] concerning the flat-band FM phase of a correlated Chern insulator described by a Haldane-Hubbard model. We considered the model at 1/4 filling of its noninteracting limit and study the system within a bosonization scheme for flat-band correlated Z_2 topological insulators. Our main result [Figs. 2(d)] is the calculation of the spin-wave excitation spectrum for the nearly flat band limit (17) of the noninteracting lower bands and equal on-site repulsion energies associated with the sublattices A and B ($U_A = U_B = U$). Moreover, we also determined the spin-wave spectrum when an offset in the on-site repulsion energies is introduced ($U_A \neq U_B$), and when the width of the lower noninteracting bands increases due to changes in the parameters of the noninteracting electronic Hamiltonian.

Differently from the correlated Chern insulator [34], for the correlated topological insulator (1), one can, in principle, define two sets of boson operators b_0 and b_1 as done in Eq. (26) considering both the spin-flip excitations (28), that changes the sublattice index (ML excitations), and the spin-flip excitations (33), that preserves the sublattice index (SL excitations). We found that the spin-wave spectrum for both ML and SL excitations are gapped and have two branches, with an energy gap between the lower and upper bands at the K and K' points of the first BZ. Such features are in contrast with the ones found for the correlated Chern insulator on a honeycomb lattice [34], whose spin-wave spectrum has a Goldstone mode at the center of the BZ (Γ point) and Dirac points at the K and K' points. Mostly important, the lowest-energy excitations are the SL ones, a feature that is distinct from the one found for the square lattice π-flux model [29], whose flat-band FM phase is characterized by ML excitations: while both correlated Chern insulators on the square [29] and honeycomb [34] lattices are characterize by the SL excitations, such a common feature seems to be not shared by the corresponding topological insulators. Finally, our findings indicated that the spin-wave bands for the SL excitations might be topologically nontrivial, even in the completely flat band limit, a feature that also contrasts with the behavior of the corresponding correlated Chern insulator [32].

ACKNOWLEDGMENTS

We thank E. Miranda for helpful discussions and L.S.G.L. kindly acknowledges the financial support of the Conselho Nacional de Desenvolvimento Científico e Tecnológico (CNPq) under the Grant No. 162323/2017-4.

APPENDIX A: THE $F_{\alpha\beta,\mathbf{q}}$ AND $\mathcal{G}_{\alpha\beta a\sigma}(\mathbf{k},\mathbf{q})$ FUNCTIONS FOR THE ML EXCITATIONS

In this Appendix, the expansions of the $F_{\alpha\beta,\mathbf{q}}$ [Eq. (31)] and the $\mathcal{G}_{\alpha\beta a\sigma}(\mathbf{k},\mathbf{q})$ functions in terms of the coefficients (12) are quoted. Such expressions were previously derived by one of us in Ref. [29].

From Eqs. (13), (14), and (32), one easily shows that Eq. (31) can be written as

$$\begin{aligned} F^2_{\alpha\beta,\mathbf{q}} = \frac{1}{4}\sum_{\mathbf{p}} & [(-1)^{\alpha} + (-1)^{\beta}](1 - \hat{B}_{3,\mathbf{p}}\hat{B}_{3,-\mathbf{p}+\mathbf{q}}) \\ & - [(-1)^{\alpha} - (-1)^{\beta}](\hat{B}_{3,\mathbf{p}} - \hat{B}_{3,-\mathbf{p}+\mathbf{p}}) \\ & + [1 + (-1)^{\alpha+\beta}](\hat{B}_{1,\mathbf{p}}\hat{B}_{1,-\mathbf{p}+\mathbf{q}} + \hat{B}_{2,\mathbf{p}}\hat{B}_{2,-\mathbf{p}+\mathbf{q}}) \\ & - i[1 - (-1)^{\alpha+\beta}](\hat{B}_{1,\mathbf{p}}\hat{B}_{2,-\mathbf{p}+\mathbf{q}} - \hat{B}_{2,\mathbf{p}}\hat{B}_{1,-\mathbf{p}+\mathbf{q}}), \end{aligned} \tag{A1}$$

where $\alpha, \beta = 0, 1$ and $\hat{B}_{i,\mathbf{k}} = B_{i,\mathbf{k}}/|\mathbf{B}_{\mathbf{k}}|$. The $F^2_{\alpha\beta,\mathbf{q}}$ function for the nearly flat band limit (17) is shown in Fig. 4. It is clear that the condition (52) is not completely fulfilled by the Haldane model (2), since $\mathrm{Im}F^2_{01,\mathbf{q}}$ and $\mathrm{Im}F^2_{10,\mathbf{q}}$ are finite in the vicinity of the M_1 and M_2 points. As discussed in Appendix B from Ref. [34], in principle, such a result indicates that it is not possible to define the two sets of independent boson operators b_0 and b_1 as done in Eq. (26), a feature that distinguishes the Haldane model (2) from the square lattice π-flux model [29]. Due to the similarities between the topological insulator (2) and the Chern insulator [34] and the fact that the bosonization scheme provides reasonable results for the correlated Chern

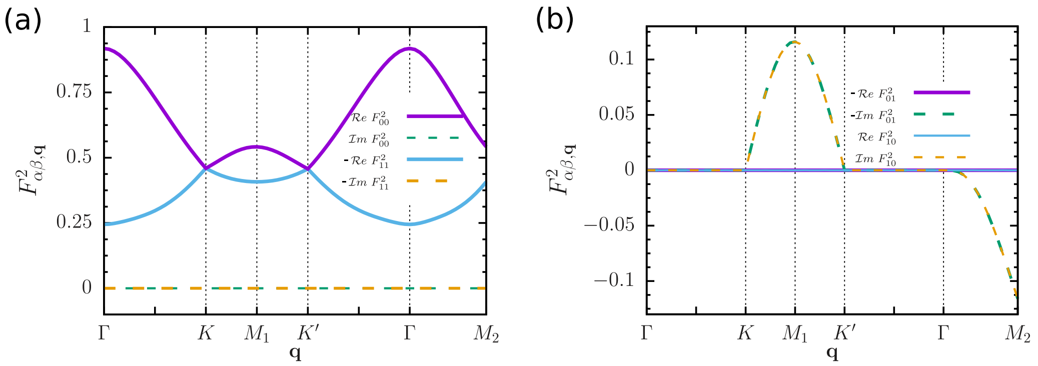

FIG. 4. ML excitations. The real (solid line) and imaginary (dashed line) parts of $F^2_{\alpha\beta,\mathbf{q}}$ [Eq. (31)] for the Haldane model (2) in the nearly-flat band limit (17) along paths in the first BZ: (a) $F^2_{00,\mathbf{q}}$ and $-F^2_{11,\mathbf{q}}$ and (b) $F^2_{01,\mathbf{q}}$ and $F^2_{10,\mathbf{q}}$.

insulator described by the Haldane-Hubbard model, we follow the lines of Ref. [34] and *assume* that, for the topological insulator (2), the bosons operators b_0 and b_1 can be defined by Eq. (26) and that they constitute two sets of independent boson operators.

Once the expansion of the $F^2_{\alpha\beta,\mathbf{q}}$ function in terms of the coefficients (12) is known, one can easily determine the kinetic coefficients (40) [compare the integrands of Eqs. (31) and (40)]. For instance, in Figs. 5(a) and 5(b), one shows the kinetic coefficients (40) for the nearly flat band limit (17).

The $\mathcal{G}_{\alpha\beta a\sigma}(\mathbf{k},\mathbf{q})$ function is defined as

$$\begin{aligned}\mathcal{G}_{\alpha\beta a\uparrow}(\mathbf{k},\mathbf{q}) &= -\sum_{\mathbf{p}} \frac{G_{a\uparrow}(\mathbf{p},\mathbf{k})}{F_{\alpha\alpha,\mathbf{q}}F_{\beta\beta,\mathbf{k}+\mathbf{q}}} g_\alpha(\mathbf{p}-\mathbf{k},\mathbf{q}) g^*_\beta(-\mathbf{p}+\mathbf{k}+\mathbf{q},\mathbf{k}+\mathbf{q}),\\ \mathcal{G}_{\alpha\beta a\downarrow}(\mathbf{k},\mathbf{q}) &= +\sum_{\mathbf{p}} \frac{G_{a\downarrow}(\mathbf{p}-\mathbf{q},\mathbf{k})}{F_{\alpha\alpha,\mathbf{q}}F_{\beta\beta,\mathbf{k}+\mathbf{q}}} g_\alpha(\mathbf{p},\mathbf{q}) g^*_\beta(-\mathbf{p}+\mathbf{k}+\mathbf{q},\mathbf{k}+\mathbf{q}),\end{aligned} \tag{A2}$$

where $G_{a\sigma}(\mathbf{p},\mathbf{q})$ is given by Eq. (23). With the aid of Eq. (14), one finds that

$$\begin{aligned}\mathcal{G}_{\alpha\beta a\sigma}(\mathbf{k},\mathbf{q}) = &- \gamma_\sigma \frac{1}{8}[\delta_{a,A} + \delta_{a,B}(-1)^{\alpha+\beta}] \frac{1}{F_{\alpha\alpha,\mathbf{q}}F_{\beta\beta,\mathbf{k}+\mathbf{q}}}\\ &\times \sum_{\mathbf{p}} \zeta_1(\sigma)[1+\gamma_\sigma(-1)^a\hat{B}_3(1)][1-\gamma_\sigma(-1)^a\hat{B}_3(2)][1-(-1)^a\hat{B}_3(3)]\\ &+ \zeta_2(\sigma)[\hat{B}_1(2)\hat{B}_1(3) + \hat{B}_2(2)\hat{B}_2(3) + i(-1)^a(\hat{B}_1(2)\hat{B}_2(3) - \hat{B}_2(2)\hat{B}_1(3))][1-(-1)^a\hat{B}_3(1)]\\ &+ \zeta_3(\sigma)[\hat{B}_1(1)\hat{B}_1(3) + \hat{B}_2(1)\hat{B}_2(3) + i(-1)^a(\hat{B}_1(1)\hat{B}_2(3) - \hat{B}_2(1)\hat{B}_1(3))][1-(-1)^a\hat{B}_3(2)]\\ &+ \zeta_4(\sigma)[\hat{B}_1(1)\hat{B}_1(2) + \hat{B}_2(1)\hat{B}_2(2) + i\gamma_\sigma(-1)^a(\hat{B}_2(1)\hat{B}_1(2) - \hat{B}_1(1)\hat{B}_2(2))][1-(-1)^a\hat{B}_3(3)],\end{aligned} \tag{A3}$$

where the coefficient $\gamma_\uparrow = -\gamma_\downarrow = 1$, the coefficients $\zeta_i(\sigma)$ read

$$\begin{aligned}&\zeta_1(\uparrow) = (-1)^\alpha, \quad \zeta_2(\uparrow) = (-1)^\beta, \quad \zeta_3(\uparrow) = 1, \quad \zeta_4(\uparrow) = (-1)^{\alpha+\beta},\\ &\zeta_1(\downarrow) = (-1)^\beta, \quad \zeta_2(\downarrow) = (-1)^{\alpha+\beta}, \quad \zeta_3(\downarrow) = (-1)^\alpha, \quad \zeta_4(\downarrow) = 1,\end{aligned} \tag{A4}$$

and the $\hat{B}_i(j)$ functions, with $i, j = 1, 2, 3$, are given by

$$\begin{aligned}&\hat{B}_i(1) = \hat{B}_{i,-\mathbf{p}+\mathbf{k}+\mathbf{q}}, \quad \hat{B}_i(2) = \hat{B}_{i,\mathbf{p}}, \quad \hat{B}_i(3) = \hat{B}_{i,+\mathbf{p}-\mathbf{k}}, \quad \text{for} \quad \sigma = \uparrow,\\ &\hat{B}_i(1) = \hat{B}_{i,-\mathbf{p}+\mathbf{k}+\mathbf{q}}, \quad \hat{B}_i(2) = \hat{B}_{i,\mathbf{p}}, \quad \hat{B}_i(3) = \hat{B}_{i,-\mathbf{p}+\mathbf{q}}, \quad \text{for} \quad \sigma = \downarrow\,.\end{aligned} \tag{A5}$$

Equations (A1) and (A3) allow us to determine the coefficients (44). In particular, the coefficients $\epsilon^{01}_{\mathbf{q}}$ and $\epsilon^{10}_{\mathbf{q}}$ for the nearly flat band limit (17) and on-site repulsion energies $U_A = U_B = U$ are plotted in Fig. 5(c). One sees that $\epsilon^{01}_{\mathbf{q}} \neq (\epsilon^{10}_{\mathbf{q}})^*$, which implies that the quadratic bosonic Hamiltonian (42) is non-Hermitian for the ML excitations (28).

APPENDIX B: THE $F_{\alpha\beta,\mathbf{q}}$ AND $\mathcal{G}_{\alpha\beta a\sigma}(\mathbf{k},\mathbf{q})$ FUNCTIONS FOR THE SL EXCITATIONS

In this Appendix, we present the equivalent of Eqs. (A1)–(A5) for the SL excitations (33). Indeed, such kind of spin-flip excitations were considered in Ref. [34] in the description of the flat-band FM phase of a correlated Chern insulator

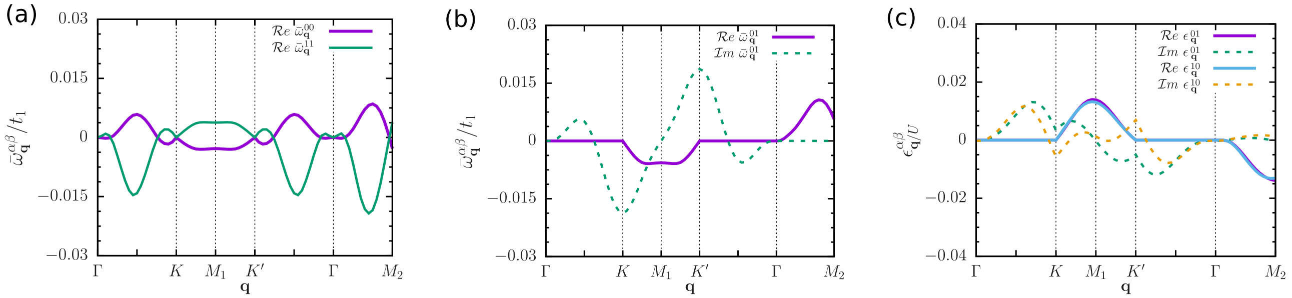

FIG. 5. ML excitations. The real (solid line) and imaginary (dashed line) parts of the kinetic coefficients (a) $\bar{\omega}^{00}_{\mathbf{q}}$ and $\bar{\omega}^{11}_{\mathbf{q}}$ and (b) $\bar{\omega}^{01}_{\mathbf{q}}$ [Eq. (40)] along paths in the first BZ for the Haldane model (2) in the nearly-flat band limit (17). (c) The real (solid line) and imaginary (dashed line) parts of the coefficients $\epsilon^{01}_{\mathbf{q}}$ and $\epsilon^{10}_{\mathbf{q}}$ [Eq. (44)] for the THM (1) in the nearly-flat band limit (17) and on-site repulsion energies $U_A = U_B = U$.

described by a Haldane-Hubbard model. However, since the canonical transformation (13) differs from the one employed in the study of the correlated Chern insulator (see Eq. (13) from Ref. [34]), the expressions of the $F_{\alpha\beta,\mathbf{q}}$ and $\mathcal{G}_{\alpha\beta a\sigma}(\mathbf{k},\mathbf{q})$ functions are distinct from the ones shown in Appendix A from Ref. [34].

From Eqs. (13), (14), and (34), one shows that, for the SL excitations, Eq. (31) assumes the form

$$
\begin{aligned}
F^2_{\alpha\beta,\mathbf{q}} =& \frac{1}{4}\sum_{\mathbf{p}}[1+(-1)^{\alpha+\beta}](1+\hat{B}_{3,\mathbf{p}}\hat{B}_{3,-\mathbf{p}+\mathbf{q}}) + [(-1)^{\alpha}+(-1)^{\beta}](\hat{B}_{1,\mathbf{p}}\hat{B}_{1,-\mathbf{p}+\mathbf{q}} - \hat{B}_{2,\mathbf{p}}\hat{B}_{2,-\mathbf{p}+\mathbf{q}})\\
&- [1-(-1)^{\alpha+\beta}](\hat{B}_{3,\mathbf{p}}+\hat{B}_{3,-\mathbf{p}+\mathbf{p}}) - i[(-1)^{\alpha}-(-1)^{\beta}](\hat{B}_{1,\mathbf{p}}\hat{B}_{2,-\mathbf{p}+\mathbf{q}}+\hat{B}_{2,\mathbf{p}}\hat{B}_{1,-\mathbf{p}+\mathbf{q}}),
\end{aligned}
\tag{B1}
$$

where $\alpha, \beta = 0, 1$ and $\hat{B}_{i,\mathbf{k}} = B_{i,\mathbf{k}}/|\mathbf{B}_{\mathbf{k}}|$. For the nearly flat band limit (17), Eq. (B1) is plotted in Figs. 6(a) and 6(b). Similarly to the ML excitations, one sees that $\mathrm{Im}F^2_{01,\mathbf{q}}$ and $\mathrm{Im}F^2_{10,\mathbf{q}}$ are finite in the vicinity of the M_1 and M_2 points, implying that the condition (52) is not satisfied by all momenta in the first BZ.

For the SL excitations, $\mathcal{G}_{\alpha\beta a\sigma}(\mathbf{k},\mathbf{q})$ is also defined by Eq. (A3), but now it reads

$$
\begin{aligned}
\mathcal{G}_{\alpha\beta a\sigma}(\mathbf{k},\mathbf{q}) =& -\gamma_{\sigma}\frac{1}{8}[\delta_{a,A}+\delta_{a,B}(-1)^{\alpha+\beta}]\frac{1}{F_{\alpha\alpha,\mathbf{q}}F_{\beta\beta,\mathbf{k}+\mathbf{q}}}\\
&\times\sum_{\mathbf{p}}[1-(-1)^{a}\hat{B}_3(1)][1-(-1)^{a}\hat{B}_3(2)][1-(-1)^{a}\hat{B}_3(3)]\\
&+\zeta_1(\sigma)[\hat{B}_1(2)\hat{B}_1(3)+\gamma_{\sigma}\hat{B}_2(2)\hat{B}_2(3)+i(-1)^{a}(\hat{B}_1(2)\hat{B}_2(3)-\gamma_{\sigma}\hat{B}_2(2)\hat{B}_1(3))][1+\gamma_{\sigma}(-1)^{a}\hat{B}_3(1)]\\
&+\zeta_2(\sigma)[\hat{B}_1(1)\hat{B}_1(3)-\gamma_{\sigma}\hat{B}_2(1)\hat{B}_2(3)+i(-1)^{a}(\hat{B}_1(1)\hat{B}_2(3)+\gamma_{\sigma}\hat{B}_2(1)\hat{B}_1(3))][1-\gamma_{\sigma}(-1)^{a}\hat{B}_3(2)]\\
&+\zeta_3(\sigma)[\hat{B}_1(1)\hat{B}_1(2)-\hat{B}_2(1)\hat{B}_2(2)-i(-1)^{a}(\hat{B}_1(1)\hat{B}_2(2)+\hat{B}_2(1)\hat{B}_1(2))][1-(-1)^{a}\hat{B}_3(3)],
\end{aligned}
\tag{B2}
$$

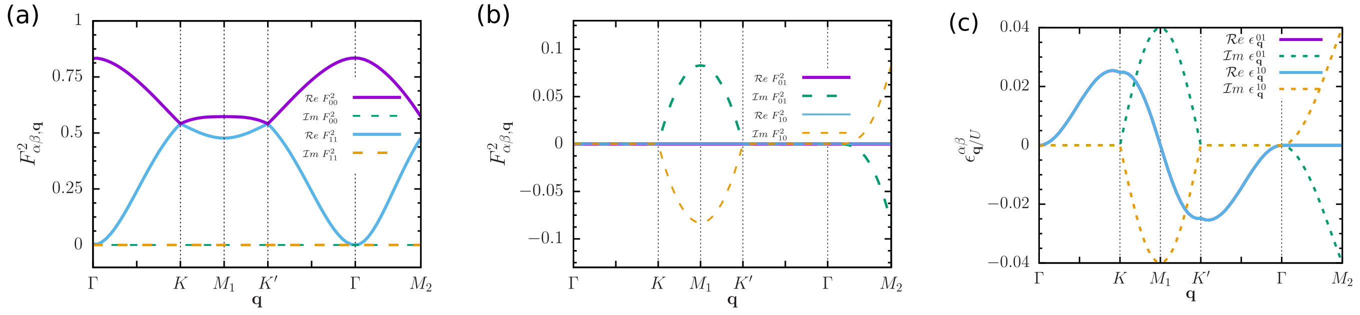

FIG. 6. SL excitations. The real (solid line) and imaginary (dashed line) parts of $F^2_{\alpha\beta,\mathbf{q}}$ [Eq. (31)] for the Haldane model (2) in the nearly-flat band limit (17) along paths in the first BZ: (a) $F^2_{00,\mathbf{q}}$ and $F^2_{11,\mathbf{q}}$ and (b) $F^2_{01,\mathbf{q}}$ and $F^2_{10,\mathbf{q}}$. (c) The real (solid line) and imaginary (dashed line) parts of the coefficients $\epsilon^{01}_{\mathbf{q}}$ and $\epsilon^{10}_{\mathbf{q}}$ [Eq. (44)] for the THM (1) in the nearly-flat band limit (17) and on-site repulsion energies $U_A = U_B = U$.

where the coefficient $\gamma_\uparrow = -\gamma_\downarrow = 1$, the coefficients $\zeta_i(\sigma)$ are given by

$$\begin{aligned} &\zeta_1(\uparrow) = (-1)^{\alpha+\beta}, \qquad \zeta_2(\uparrow) = (-1)^{\alpha}, \qquad \zeta_3(\uparrow) = (-1)^{\beta}, \\ &\zeta_1(\downarrow) = (-1)^{\alpha}, \qquad \zeta_2(\downarrow) = (-1)^{\alpha+\beta}, \qquad \zeta_3(\downarrow) = (-1)^{\beta}, \end{aligned} \tag{B3}$$

and the $\hat{B}_i(j)$ functions, with $i, j = 1, 2, 3$, are defined as

$$\begin{aligned} &\hat{B}_i(1) = \hat{B}_{i,-\mathbf{p}+\mathbf{k}+\mathbf{q}}, \qquad \hat{B}_i(2) = \hat{B}_{i,\mathbf{p}}, \qquad \hat{B}_i(3) = \hat{B}_{i,+\mathbf{p}-\mathbf{k}}, \qquad \text{for} \quad \sigma = \uparrow, \\ &\hat{B}_i(1) = \hat{B}_{i,-\mathbf{p}+\mathbf{k}+\mathbf{q}}, \qquad \hat{B}_i(2) = \hat{B}_{i,\mathbf{p}}, \qquad \hat{B}_i(3) = \hat{B}_{i,-\mathbf{p}+\mathbf{q}}, \qquad \text{for} \quad \sigma = \downarrow. \end{aligned} \tag{B4}$$

With the aid of Eqs. (B1) and (B2), one can calculate the coefficients (44). For instance, the coefficients $\epsilon^{01}_{\mathbf{q}}$ and $\epsilon^{10}_{\mathbf{q}}$ for the nearly flat band limit (17) and on-site repulsion energies $U_A = U_B = U$ are shown in Fig. 6(c). Since $\epsilon^{01}_{\mathbf{q}} = (\epsilon^{10}_{\mathbf{q}})^*$, the quadratic bosonic Hamiltonian (42) is Hermitian for the SL excitations (33).

APPENDIX C: SPIN-WAVE SPECTRUM FOR THE ML EXCITATIONS

Here we discuss in details the behavior of the spin-wave spectrum (50) for the ML excitations (28). In this case, one should consider the expressions of $g_\alpha(\mathbf{p}, \mathbf{q})$, $F_{\alpha\beta,\mathbf{q}}$, and $\mathcal{G}_{\alpha\beta\alpha\sigma}(\mathbf{p}, \mathbf{q})$ respectively given by Eqs. (32), (A1), and (A3) in order to determine the kinetic coefficients (40) and the coefficients (44).

Before discussing the behavior of the spin-wave spectrum for the ML excitations, a few remarks here about the dispersion relation (50) are in order: (i) We follow the procedure adopted in our previous study [34] for the flat-band FM phase of a correlated Chern insulator described by a Haldane-Hubbard model, and completely neglect the contribution of the kinetic coefficients (40); indeed, for the ML excitations, we find that $\bar{\omega}^{\alpha\alpha}_{\mathbf{q}}$ are real while $\bar{\omega}^{01}_{\mathbf{q}}$ and $\bar{\omega}^{10}_{\mathbf{q}}$ are finite complex quantities, but rather small in units of the nearest-neighbor hopping energy t_1 [see Figs. 5(a) and 5(b)]; as discussed in detail in Ref. [34], we believe that such finite values for $\bar{\omega}^{\alpha\beta}_{\mathbf{q}}$ are related to the symmetries of the Haldane model (2) and to the fact that the condition (52) is not fulfilled for all momenta $\mathbf{q}$ within the first BZ (see Fig. 4). (ii) Concerning the coefficients (44), we find that they are also complex quantities, with $\epsilon^{\alpha\alpha}_{\mathbf{q}}$ having a quite small imaginary part and $\epsilon^{01}_{\mathbf{q}} \neq (\epsilon^{10}_{\mathbf{q}})^*$ as shown in Fig. 5(c); such features imply that the quadratic Hamiltonian (42) is non-Hermitian, a behavior previously found for the correlated Chern insulator [34]; at the moment, we believe that the non-Hermiticity of the Hamiltonian (42) might be an artifact of the bosonization formalism associated with the fact that the condition (52) is not completely satisfied by the Haldane model (2); however, for the correlated Chern insulator [34], the presence of the off-diagonal terms $(\alpha, \beta) = (0, 1)$ and (1,0) of the quadratic bosonic Hamiltonian (42) are indeed important, since they yield a spin-wave spectrum with Dirac points at the K and K' points of the first BZ (see Fig. 6 from Ref. [34]), in agreement with the numerical calculations [32]; therefore, for the ML excitations, we also consider the complete and non-Hermitian quadratic Hamiltonian (42). For more details about these two important issues, we refer the reader to Sec. VI B and Appendix B from Ref. [34].

Figure 2(a) shows the dispersion relation (50) for the nearly flat band limit (17) and on-site repulsion energies $U_A = U_B = U$. One sees that the spin-wave spectrum for the ML excitations is gapped and has two branches: the gap of the lower branch is at the M_i points of the first BZ while the gap of the upper one is at the K and K' points. Small energy gaps between the lower and upper bands at the K and K' points are found,

$$\Delta^{(K)} = \Omega_{+,K} - \Omega_{-,K} = 1.04 \times 10^{-2}\, U, \tag{C1}$$

in contrast with the corresponding correlated Chern insulator [34], whose spin-wave spectrum displays Dirac points at the K and K' points. Due to the non-Hermiticity of the quadratic boson term (42), one finds that the spin-wave excitations (50) have a quite small decay rate (the imaginary part of $\Omega_{\pm,\mathbf{q}}$) along the K-M_1-K' line, i.e., at the border of the first BZ [see the dashed line in Fig. 2(a) and note the multiplicative factor 20]. Such a feature was also found in the study of the correlated Chern insulator in Ref. [34].

The spin-wave spectra (50) for the nearly flat-band limit (17) and on-site repulsion energies $U_B = 0.8\, U_A = 0.8\, U$ and $U_B = 0.6\, U_A = 0.6\, U$ are shown in Figs. 2(b) and 2(c), respectively. One sees that, as the diference $\Delta U = U_A - U_B$ increases: The energies of the spin-wave excitations decrease; the energy gap between the lower and upper bands at the K point increases,

$$\begin{aligned} \Delta^{(K)} &= 1.95 \times 10^{-2}\, U \quad \text{for} \quad \Delta U = 0.2\, U, \\ \Delta^{(K)} &= 2.85 \times 10^{-2}\, U \quad \text{for} \quad \Delta U = 0.4\, U, \end{aligned}$$

while the energy gap at the K' point also varies,

$$\begin{aligned} \Delta^{(K')} &= 6.97 \times 10^{-4}\, U \quad \text{for} \quad \Delta U = 0.2\, U, \\ \Delta^{(K')} &= 1.12 \times 10^{-2}\, U \quad \text{for} \quad \Delta U = 0.4\, U. \end{aligned}$$

For $U_B > U_A$ (not shown here), similar features are observed, but now the energy gap at the K' point increases instead of the one at K point with the same overall intensities. Similarly to the homogeneous configuration $U_A = U_B = U$, the spin-wave excitations (50) at the border of the first BZ also have finite decay rates, which decrease as the diference $\Delta U = U_A - U_B$ increases.

The behavior of the spin-wave spectrum (50) when the THM (1) is moved away from the nearly flat band limit (17) was also considered. One calculates the spin-wave spectrum (50) for $\phi = 0.4, 0.5, 0.7$, and 0.8, hopping amplitude t_2 given by the relation $\cos(\phi) = t_1/(4t_2)$, and homogeneous on-site repulsion energies $U_A = U_B = U$ (not shown here). Similarly to the SL excitations [Figs. 3(a) and 3(b)], one finds that the

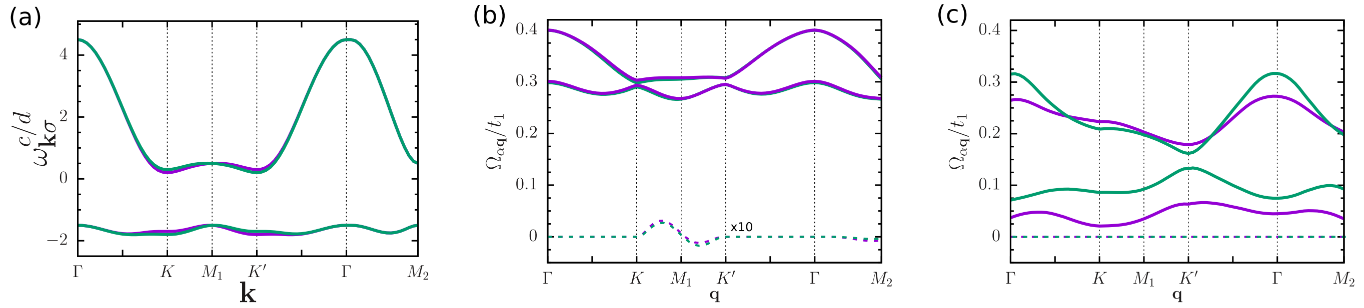

FIG. 7. (a) Free electronic band structure (16) with the additional staggered on-site energy term (D1) along paths in the first BZ [Fig. 1(b)] for the nearly flat band limit (17) and staggered on-site energy $M = 0.1\,t_1$: $\sigma =\uparrow$ (magenta) and $\sigma =\downarrow$ (green). (b) ML excitations (28). Spin-wave spectrum (50) along paths in the first BZ for the nearly flat band limit (17), on-site Hubbard repulsion energies $U_A = U_B = U$, and staggered on-site energy $M = 0.05$ (green) and $M = 0.1\,t_1$ (magenta); solid and dashed lines respectively represent the real part of $\Omega_{\pm,\mathbf{q}}$ and the imaginary part of $\Omega_{+,\mathbf{q}} = -\Omega_{-,\mathbf{q}}$, where the latter is multiplied by a factor of 10 for clarity. (c) Similar to panel (b), but for the SL excitations (33).

spin-wave spectra are quite similar to the one obtained for the nearly-flat band limit (17), $\phi = 0.656$.

Even though the ML excitations are not the lowest-energy ones for the correlated topological insulator (1), it would be interesting to see whether the linear combinations (28) and (33) could be slightly modified (e.g., with momentum dependent coefficients) such that the condition (52) is now satisfied by all momenta in the first BZ. Such an modification may yield an Hermitian effective boson model not only for the ML excitations, but also for the SL excitations of the correlated Chern insulator [34]. We left this issue for a future work.

APPENDIX D: STAGGERED ON-SITE ENERGY TERM

Here we briefly comment on the effects on the spin-wave spectrum (50) due to the presence of an staggered on-site energy term,

$$H_M = \sum_{i\sigma} M(c^\dagger_{iA\sigma}c_{iA\sigma} - c^\dagger_{iB\sigma}c_{iB\sigma}), \tag{D1}$$

which breaks inversion symmetry when added to the noninteracting model (2). In the presence of the term (D1), it is easy to see that the Hamiltonian (2) also assumes the form (15), with the dispersion of the free-electronic bands given by Eq. (16) apart from the modification

$$B^\sigma_{3,\mathbf{k}} \rightarrow B^\sigma_{3,\mathbf{k}} + M = \gamma_\sigma B_{3,\mathbf{k}} + M. \tag{D2}$$

As discussed in detail in Sec. II B from Ref. [34], a finite on-site energy M increases the bandwidth of the lower free-electronic band c, i.e., it allows us to move away from the nearly flat-band limit, keeping the optimal parameter choice (17) for t_2 and ϕ. Distinct from the Chern insulator on the hexagonal lattice [34], the staggered on-site energy term (D1) breaks the symmetry between the spin ↑ and the spin ↓ free-electronic bands as illustrated in Fig. 7(a) [note the γ_σ factor in Eq. (D2)].

Figures 7(b) and 7(c) show the spin-wave spectrum (50) for t_2 and ϕ given by the optimal parameter choice (17), staggered on-site energy $M = 0.05$ and $0.1\,t_1$, and on-site repulsion energies $U_A = U_B = U = t_1$. For the ML excitations (28) [Fig. 7(b)], a finite $M = 0.05\,t_1$ yields minor effects on the spin-wave spectrum as compared with the homogenous case $M = 0$ [Fig. 2(a)]. Even for $M = 0.1\,t_1$, the effects remain small, with just a decreasing of the spin-wave energies around the K point and an increasing in the energy gap between the lower and the upper bands at the K' point. Also, the decay rates (the imaginary part of $\Omega_{\pm,\mathbf{q}}$) display quite little modifications due to a finite M. On the other hand, for the SL excitations (33), the effects related to a finite M are more pronounced; see Fig. 7(c). Comparing with the homogeneous case $M = 0$ [Fig. 2(d)], one notices that, as M increases: The energy gap between the lower and upper bands increases at the K point and it has a nonmonotonic behavior at the K' point; the excitation gap of the lower band decreases and it moves from the Γ point to the K one. Such effects are qualitatively similar to the ones found for on-site repulsion energies $U_A \neq U_B$; see Figs. 2(e) and 2(f). Interestingly, for $M = 0.1\,t_1$, the excitation energy almost vanishes at the K point, a feature that could indicate an instability of the flat-band FM phase. One should mention that, for the correlated Chern insulator [34], an instability of the flat-band FM phase was found for any finite M. Finally, one should point out that, for $M < 0$ (not shown here), the modifications in the spin-wave spectrum in the vicinity of the K and K' points are reversed.

The fact that the energy of the excitation gap monotonically decreases as M increases, as found for the SL excitations, was previously observed for a time-reversal symmetric THM on a square lattice [28].

APPENDIX E: CHERN NUMBERS OF THE SPIN-WAVE BANDS

In this Appendix, we briefly describe the procedure employed to numerically calculate the Chern numbers of the spin-wave bands (50).

We start casting the effective quadratic boson model (42) in a matrix form as done in Sec. II B for the noninteracting Hamiltonian (2),

$$\bar{H}^{(2)}_{U,B} = \sum_{\mathbf{q}} \Phi^\dagger_{\mathbf{q}} \tilde{h}_{\mathbf{q}} \Phi_{\mathbf{q}}, \tag{E1}$$

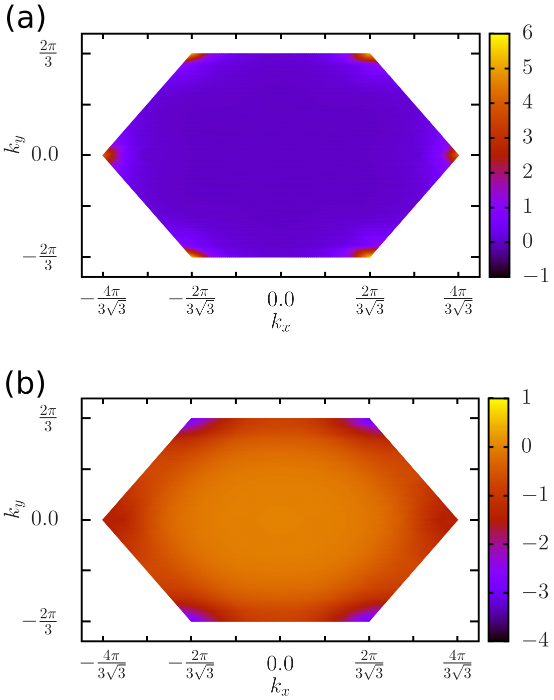

FIG. 8. Contour plot of the Berry curvature of the lower spin-wave band within the first BZ for the nearly flat band limit (17) and on-site repulsion energies $U_A = U_B = U$. (a) ML [Fig. 2(a)] and (b) SL [Fig. 2(d)] excitations.

where the two-component spinor $\Phi_{\mathbf{k}} = (b_{0,\mathbf{q}} \;\; b_{1,\mathbf{q}})^T$, and the 2×2 matrix $\tilde{h}_{\mathbf{q}}$ assumes the form

$$\tilde{h}_{\mathbf{q}} = \tilde{B}_{0,\mathbf{q}}\tau_0 + \sum_{\mu=1}^{3} \tilde{B}_{\mu,\mathbf{q}}\tau_\mu. \tag{E2}$$

Here τ_0 is the identity matrix, τ_μ is a Pauli matrix, and

$$\tilde{B}_{0,\mathbf{q}} = \frac{1}{2}\left(\epsilon^{00}_{\mathbf{q}} + \epsilon^{11}_{\mathbf{q}}\right), \qquad \tilde{B}_{1,\mathbf{q}} = \frac{1}{2}\left(\epsilon^{01}_{\mathbf{q}} + \epsilon^{10}_{\mathbf{q}}\right),$$
$$\tilde{B}_{2,\mathbf{q}} = \frac{1}{2i}\left(\epsilon^{01}_{\mathbf{q}} - \epsilon^{10}_{\mathbf{q}}\right), \qquad \tilde{B}_{3,\mathbf{q}} = \frac{1}{2}\left(\epsilon^{00}_{\mathbf{q}} - \epsilon^{11}_{\mathbf{q}}\right), \tag{E3}$$

with $\epsilon^{\alpha\beta}_{\mathbf{q}}$ being the coefficients (44).

Due to the similarities between the forms of the Hamiltonians (8) and (E1), the Chern numbers of the spin-wave bands (50) are also given by Eq. (18), apart from the γ_σ factor and the replacement $\hat{B}_{\mu,\mathbf{k}} \to \tilde{B}_{\mu,\mathbf{k}}/|\tilde{\mathbf{B}}_{\mathbf{k}}|$, where $|\tilde{\mathbf{B}}_{\mathbf{k}}| = \sqrt{\tilde{B}^2_{1,\mathbf{k}} + \tilde{B}^2_{2,\mathbf{k}} + \tilde{B}^2_{3,\mathbf{k}}}$. Moreover, for the ML excitations, we assume that $\epsilon^{01}_{\mathbf{q}} = (\epsilon^{10}_{\mathbf{q}})^*$ in order to obtain real Chern numbers: Recall that, only for the ML excitations, the quadratic Hamiltonian (42) is non-Hermitian, see Appendix C; such an assumption was also made in Ref. [34] in order to determine the Chern numbers of the spin-wave bands of a correlated Chern insulator.

The Berry curvature, which is defined as one-half of the integrand of Eq. (18), of the lower spin-wave band (50) for the nearly flat-band limit (17) and on-site repulsion energies $U_A = U_B = U$ is shown in Fig. 8. For both ML and SL excitations, one sees that the Berry curvatures peak at the K and K' points of the first BZ.

The Chern numbers of the lower spin-wave bands (50) for both the ML (C_{ML}) and the SL (C_{SL}) excitations, which are determined by numerically integrating Eq. (18) and considering the coefficients (E3), are shown in Table I. For the SL excitations shown in Figs. 2(d) and 2(e), one sees that the Chern numbers are close to one. We believe that the small deviations from the unit might be due to the fact that the numerical procedure used to calculated the Chern numbers does not properly take into account the behavior of the Berry curvature [Fig. 8(b)] at the corners of the first BZ. On the other hand, for the ML excitations shown in Figs. 2(a) and 2(b), the Chern numbers are finite, but smaller than one. In addition to possible numerical issues [see Fig. 8(a)], such fractional values for the Chern numbers might also be associated to the fact that it is necessary to assume that $\epsilon^{01}_{\mathbf{q}} = (\epsilon^{10}_{\mathbf{q}})^*$ in order to obtain real Chern numbers.

The nonzero Chern numbers found for the spin-wave bands of the correlated topological insulator are in constrast with the topological properties of the corresponding correlated Chern insulator on a honeycomb lattice [32,34]. In the completely flat band limit, i.e, when the dispersion of the noninteracting electronic bands is neglected (an approximation similar to the assumption $\bar{\omega}^{\alpha\beta}_{\mathbf{q}} = 0$ made in Appendix C and in Ref. [34] that the kinetic coefficients (40) vanish), it was found that the spin-wave bands of the correlated Chern insulator are topologically trivial [32,34]. Indeed, our previous results [34] are in agreement with the exact diagonalization calculations [32]. Moreover, it was also numerically shown [32] that the spin-wave bands of the correlated Chern insulator acquire nonzero Chern numbers when the dispersion of the free-electronic bands is explicitly taken into account (see also Sec. V from Ref. [34]).

Although it is not clear whether the spin-wave bands for the ML excitations (28) are topologically nontrivial, one finds some evidences that the spin-wave bands for the SL excitations (33) might be topologically nontrivial, even in the completely flat band limit of the free-electronic bands, a feature that contrasts with the behaviour of the corresponding correlated Chern insulator.

---

[1] F. D. M. Haldane, Model for a Quantum Hall Effect without Landau Levels: Condensed-Matter Realization of the "Parity Anomaly", Phys. Rev. Lett. **61**, 2015 (1988).

[2] D. J. Thouless, M. Kohmoto, M. P. Nightingale, and M. den Nijs, Quantized Hall Conductance in a Two-Dimensional Periodic Potential, Phys. Rev. Lett. **49**, 405 (1982).

[3] X.-L. Qi and S.-C. Zhang, Topological insulators and superconductors, Rev. Mod. Phys. **83**, 1057 (2011).

[4] C.-Z. Chang, C.-X. Liu, and A. H. MacDonald, Quantum anomalous Hall effect, arxiv:2202.13902.

[5] C. L. Kane and E. J. Mele, Z_2 Topological Order and the Quantum Spin Hall Effect, Phys. Rev. Lett. **95**, 146802 (2005).

[6] C. L. Kane and E. J. Mele, Quantum Spin Hall Effect in Graphene, Phys. Rev. Lett. **95**, 226801 (2005).

[7] M. Z. Hasan and C. L. Kane, Colloquium: Topological insulators, Rev. Mod. Phys. **82**, 3045 (2010).

[8] C. L. Kane, in *Topological Insulators*, Contemporary Concepts of Condensed Matter Science Vol. 6, edited by M. Franz and L. Molenkamp (Elsevier, Oxford, UK, 2013), p. 3.

[9] B. A. Bernevig and S.-C. Zhang, Quantum Spin Hall Effect, Phys. Rev. Lett. **96**, 106802 (2006).

[10] B. A. Bernevig, T. L. Hughes, and S.-C. Zhang, Quantum spin hall effect and topological phase transition in HgTe quantum wells, Science **314**, 1757 (2006).

[11] M. König, S. Wiedmann, C. Brüne, A. Roth, H. Buhmann, L. W. Molenkamp, X. L. Qi, and S. C. Zhang, Quantum spin Hall insulator state in HgTe quantum wells, Science **318**, 766 (2007).

[12] N. Goldman, J. C. Budich, and P. Zoller, Topological quantum matter with ultracold gases in optical lattices, Nat. Phys. **12**, 639 (2016).

[13] D.-W. Zhang, Y.-Q. Zhu, Y. X. Zhao, H. Yan, and S.-L. Zhu, Topological quantum matter with cold atoms, Adv. Phys. **67**, 253 (2018).

[14] N. R. Cooper, J. Dalibard, and I. B. Spielman, Topological bands for ultracold atoms, Rev. Mod. Phys. **91**, 015005 (2019).

[15] M. Hohenadler and F. F. Assaad, Correlation effects in two-dimensional topological insulators, J. Phys.: Condens. Matter **25**, 143201 (2013).

[16] S. Rachel, Interacting topological insulators: A review, Rep. Prog. Phys. **81**, 116501 (2018).

[17] S. Rachel and K. Le Hur, Topological insulators and Mott physics from the Hubbard interaction, Phys. Rev. B **82**, 075106 (2010).

[18] M. Hohenadler, T. C. Lang, and F. F. Assaad, Correlation Effects in Quantum Spin-Hall Insulators: A Quantum Monte Carlo Study, Phys. Rev. Lett. **106**, 100403 (2011).

[19] S.-L. Yu, X. C. Xie, and J.-X. Li, Mott Physics and Topological Phase Transition in Correlated Dirac Fermions, Phys. Rev. Lett. **107**, 010401 (2011).

[20] D. Zheng, G.-M. Zhang, and C. Wu, Particle-hole symmetry and interaction effects in the Kane-Mele-Hubbard model, Phys. Rev. B **84**, 205121 (2011).

[21] M. Hohenadler, Z. Y. Meng, T. C. Lang, S. Wessel, A. Muramatsu, and F. F. Assaad, Quantum phase transitions in the Kane-Mele-Hubbard model, Phys. Rev. B **85**, 115132 (2012).

[22] H.-H. Hung, L. Wang, Z.-C. Gu, and G. A. Fiete, Topological phase transition in a generalized Kane-Mele-Hubbard model: A combined quantum Monte Carlo and Green's function study, Phys. Rev. B **87**, 121113(R) (2013).

[23] T. C. Lang, A. M. Essin, V. Gurarie, and S. Wessel, Z_2 topological invariants in two dimensions from quantum Monte Carlo, Phys. Rev. B **87**, 205101 (2013).

[24] H.-H. Hung, V. Chua, L. Wang, and G. A. Fiete, Interaction effects on topological phase transitions via numerically exact quantum Monte Carlo calculations, Phys. Rev. B **89**, 235104 (2014).

[25] M. Laubach, J. Reuther, R. Thomale, and S. Rachel, Rashba spin-orbit coupling in the Kane-Mele-Hubbard model, Phys. Rev. B **90**, 165136 (2014).

[26] J. Hutchinson, P. W. Klein, and K. Le Hur, Analytical approach for the Mott transition in the Kane-Mele-Hubbard model, Phys. Rev. B **104**, 075120 (2021).

[27] H. Katsura, I. Maruyama, A. Tanaka, and H. Tasaki, Ferromagnetism in the Hubbard model with topological/non-topological flat bands, Europhys. Lett. **91**, 57007 (2010).

[28] T. Neupert, L. Santos, S. Ryu, C. Chamon, and C. Mudry, Topological Hubbard Model and Its High-Temperature Quantum Hall Effect, Phys. Rev. Lett. **108**, 046806 (2012).

[29] R. L. Doretto and M. O. Goerbig, Flat-band ferromagnetism and spin waves in topological Hubbard models, Phys. Rev. B **92**, 245124 (2015).

[30] X.-F. Su, Z.-L. Gu, Z.-Y. Dong, and J.-X. Li, Topological magnons in a one-dimensional itinerant flatband ferromagnet, Phys. Rev. B **97**, 245111 (2018).

[31] X.-F. Su, Z.-L. Gu, Z.-Y. Dong, S.-L. Yu, and J.-X. Li, Ferromagnetism and spin excitations in topological Hubbard models with a flat band, Phys. Rev. B **99**, 014407 (2019).

[32] Z.-L. Gu, Z.-Y. Dong, S.-L. Yu, J.-X. Li, Itinerant topological magnons in Haldane Hubbard model with a nearly-flat electron band, arXiv:1908.09255.

[33] Z.-L. Gu, J.-X. Li, Itinerant topological magnons in SU(2) symmetric topological hubbard models with nearly flat electronic bands, Chin. Phys. Lett. **38**, 057501 (2021).

[34] L. S. G. Leite and R. L. Doretto, Flat-band ferromagnetism and spin waves in the Haldane-Hubbard model, Phys. Rev. B **104**, 155129 (2021).

[35] K. Kusakabe and H. Aoki, Ferromagnetic Spin-Wave Theory in the Multiband Hubbard Model Having a Flat Band, Phys. Rev. Lett. **72**, 144 (1994).

[36] H. Tasaki, Stability of ferromagnetism in Hubbard models with nearly flat bands, J. Stat. Phys. **84**, 535 (1996).

[37] For reviews on flat band ferromagnetism see, e.g., H. Tasaki, From Nagaoka's FM to flat band FM and beyond, Prog. Theor. Phys. **99**, 489 (1998); Hubbard model and the origin of ferromagnetism, Eur. Phys. J. B **64**, 365 (2008).

[38] T. Neupert, L. Santos, C. Chamon, and C. Mudry, Fractional Quantum Hall States at Zero Magnetic Field, Phys. Rev. Lett. **106**, 236804 (2011).

[39] K. Sun, Z. Gu, H. Katsura, and S. Das Sarma, Nearly Flatbands with Nontrivial Topology, Phys. Rev. Lett. **106**, 236803 (2011).

[40] E. Tang, J.-W. Mei, and X.-G. Wen, High-Temperature Fractional Quantum Hall States, Phys. Rev. Lett. **106**, 236802 (2011).

[41] R. L. Doretto, A. O. Caldeira and S. M. Girvin, Lowest Landau level bosonization, Phys. Rev. B **71**, 045339 (2005).

[42] The directions of the red dashed arrows in Fig. 1(a) from Ref. [34] are not correct. The schematic representation shown here in Fig 1(a) is consistent with the Hamiltonian (2).

[43] See Sec. III B from C.-K. Chiu, J. C. Y. Teo, A. P. Schnyder, and S. Ryu, Classification of topological quantum matter with symmetries, Rev. Mod. Phys. **88**, 035005 (2016).